

Reconstruction of atmospheric neutrinos in DUNE's horizontal-drift far-detector module

S. Abbaslu¹¹⁴, F. Abd Alrahman⁸¹, A. Abed Abud³⁵, R. Acciarri³⁵,
 L. P. Accorsi¹⁹³, M. A. Acero¹², M. R. Adames¹⁹³, G. Adamov⁷²,
 M. Adamowski⁶⁶, C. Adriano³⁰, F. Akbar¹⁷⁶, F. Alemano⁹⁸, N. S. Alex¹⁷⁶,
 K. Allison⁴³, M. Alrashed¹²³, A. Alton¹³, R. Alvarez³⁹, T. Alves⁸⁹, A. Aman⁶⁹,
 H. Amar⁸⁴, P. Amedo^{85,84}, J. Anderson⁸, D. A. Andrade⁸⁸, C. Andreopoulos¹³¹,
 M. Andreotti^{95,67}, M. P. Andrews⁶⁶, F. Andrianala⁵, S. Andringa¹³⁰,
 F. Anjarazafy⁵, S. Ansarifard¹¹⁴, D. Antic¹⁹, M. Antoniassi¹⁹³,
 A. Aranda-Fernandez⁴², T. Araya-Santander³², L. Arellano¹³⁷, E. Arrieta
 Diaz¹⁸¹, M. A. Arroyave⁶⁶, M. Arteropons¹⁵⁹, J. Asaadi¹⁹⁷, M. Ascencio¹¹²,
 A. Ashkenazi¹⁹⁴, D. Asner²⁰, L. Asquith¹⁹¹, E. Atkin⁸⁹, D. Auguste¹⁶¹,
 A. Aurisano⁴⁰, V. Aushev¹²⁷, D. Autiero¹¹³, D. Ávila Gómez⁵⁸, M. B. Azam⁸⁸,
 F. Azfar¹⁵⁷, A. Back⁹², J. J. Back²¹⁰, Y. Bae¹⁴⁵, I. Bagaturia⁷², L. Bagby⁶⁶,
 D. Baigarashov², S. Balasubramanian⁶⁶, A. Balboni^{67,95}, P. Baldi²⁴,
 W. Baldini⁹⁵, J. Baldonedo²⁰⁷, B. Baller⁶⁶, B. Bambah⁸², F. Barao^{130,116},
 D. Barbu²¹, G. Barenboim⁸⁴, P. Barham Alzás³⁵, G. J. Barker²¹⁰,
 W. Barkhouse¹⁵⁰, G. Barr¹⁵⁷, A. Barros¹⁹³, N. Barros^{130,61}, D. Barrow¹⁵⁷,
 J. L. Barrow¹⁴⁵, A. Basharina-Freshville²⁰³, A. Bashyal²⁰, V. Basque⁶⁶,
 M. Bassani¹⁰⁰, D. Basu¹⁵¹, C. Batchelor⁵⁷, L. Bathe-Peters¹⁵⁷, J.B.R. Battat²¹¹,
 F. Battisti⁹³, J. Bautista¹⁴⁵, F. Bay⁴, J. L. L. Bazo Alba¹⁷⁰, J. F. Beaom¹⁵⁵,
 E. Bechettoille¹¹³, B. Behera¹⁸⁷, E. Belchior¹³³, B. Bell⁵⁴, G. Bell⁵²,
 L. Bellantoni⁶⁶, G. Bellettini^{104,168}, V. Bellini^{94,31}, O. Beltramello³⁵,
 A. Belyaev²¹⁶, C. Benitez Montiel^{84,10}, D. Benjamin²⁰, F. Bento Neves¹³⁰,
 J. Berger⁴⁴, S. Berkman¹⁴¹, J. Bermudez¹⁰², J. Bernal¹⁰, P. Bernardini^{98,180},
 A. Bersani⁹⁷, E. Bertholet¹⁹⁴, E. Bertolini⁹⁹, S. Bertolucci^{93,17}, M. Betancourt⁶⁶,
 A. Betancur Rodríguez⁵⁸, Y. Bezawada²³, A. T. Bezerra⁶², A. Bhat³⁷,
 V. Bhatnagar¹⁶⁰, M. Bhattacharjee⁹⁰, S. Bhattacharjee¹³³, M. Bhattacharya⁶⁶,
 S. Bhuller¹⁵⁷, B. Bhuyan⁹⁰, S. Biagi¹⁰⁷, J. Bian²⁴, K. Biery⁶⁶, B. Bilki^{15,111},
 M. Bishai²⁰, P. Bishop²¹³, A. Blake¹²⁸, F. D. Blaszczyk⁶⁶, G. C. Blazey¹⁵¹,
 E. Blucher³⁷, A. Bodek¹⁷⁶, B. Bogart¹⁴⁰, J. Boissevain¹³², S. Bolognesi³⁴,
 T. Bolton¹²³, L. Bomben^{99,110}, M. Bonesini^{99,142}, C. Bonilla-Diaz³², A. Booth¹⁷³,
 F. Boran⁹², C. Borden⁹², R. Borges Merlo³⁰, N. Bostan¹¹¹, G. Botogoske¹⁰¹,
 B. Bottino^{97,71}, R. Bouet¹³⁴, J. Boza⁴⁴, J. Bracinik¹⁶, B. Brahma⁹¹,
 D. Brailsford¹²⁸, F. Bramati⁹⁹, A. Branca⁹⁹, A. Brandt¹⁹⁷, J. Bremer³⁵,

S. J. Brice⁶⁶, V. Brio⁹⁴, C. Brizzolari^{99,142}, C. Bromberg¹⁴¹, J. Brooke¹⁹,
 A. Bross⁶⁶, G. Brunetti^{99,142}, M. B. Brunetti²⁰⁴, N. Buchanan⁴⁴, H. Budd¹⁷⁶,
 J. Buergi¹⁴, A. Bundock¹⁹, D. Burgardt²¹², S. Butchart¹⁹¹, G. Caceres V.²³,
 R. Calabrese¹⁰¹, R. Calabrese^{95,67}, J. Calcutt^{20,156}, L. Calivers¹⁴, E. Calvo³⁹,
 A. Caminata⁹⁷, A. F. Camino¹⁶⁹, W. Campanelli¹³⁰, A. Campani^{97,71},
 A. Campos Benitez²⁰⁸, N. Canci¹⁰¹, J. Capó⁸⁴, I. Caracas¹³⁶, D. Caratelli²⁷,
 D. Carber⁴⁴, J. M. Carceller³⁵, G. Carini²⁰, B. Carlus¹¹³, M. F. Carneiro²⁰,
 P. Carniti^{99,142}, I. Caro Terrazas⁴⁴, H. Carranza¹⁹⁷, N. Carrara²³, L. Carroll¹²³,
 T. Carroll²¹⁴, A. Carter¹⁷⁷, E. Casarejos²⁰⁷, D. Casazza⁹⁵, J. F. Castaño Forero⁷,
 F. A. Castaño⁶, C. Castromonte¹⁰⁹, E. Catano-Mur²¹³, C. Cattadori⁹⁹,
 F. Cavalier¹⁶¹, F. Cavanna⁶⁶, E. F. Ceceña-Avendaño⁴¹, S. Centro¹⁵⁹,
 G. Cerati⁶⁶, C. Cerna¹¹⁵, A. Cervelli⁹³, A. Cervera Villanueva⁸⁴, J. Chakrani¹²⁹,
 M. Chalifour³⁵, A. Chappell²¹⁰, A. Chatterjee¹⁶⁷, B. Chauhan¹¹¹, C. Chavez
 Barajas¹³¹, H. Chen²⁰, M. Chen²⁴, W. C. Chen¹⁹⁹, Y. Chen¹⁸⁵, Z. Chen²⁴,
 D. Cherdack⁸¹, S. S. Chhhiba¹⁷³, C. Chi⁴⁵, F. Chiapponi⁹³, R. Chirco⁸⁸,
 N. Chitirasreemadam^{104,168}, K. Cho¹²⁶, S. Choate¹¹¹, G. Choi¹⁷⁶, D. Chokheli⁷²,
 P. S. Chong⁴⁵, B. Chowdhury⁸, D. Christian⁶⁶, M. Chung²⁰², E. Church¹⁵⁸,
 M. F. Cicala²⁰³, M. Cicerchia¹⁵⁹, V. Cicero^{93,17}, R. Ciolini¹⁰⁴, P. Clarke⁵⁷,
 G. Cline¹²⁹, A. G. Cocco¹⁰¹, J. A. B. Coelho¹⁶², A. Cohen¹⁶², J. Collazo²⁰⁷,
 J. Collot⁷⁶, H. Combs²⁰⁸, J. M. Conrad¹³⁸, L. Conti¹⁰⁶, T. Contreras⁶⁶,
 M. Convery¹⁸⁵, K. Conway¹⁸⁹, S. Copello¹⁰³, P. Cova^{100,163}, C. Cox¹⁷⁷,
 L. Cremonesi¹⁷³, J. I. Crespo-Anadón³⁹, M. Crisler⁶⁶, E. Cristaldo^{99,10},
 J. Crnkovic⁶⁶, G. Crone²⁰³, R. Cross²¹⁰, A. Cudd⁴³, C. Cuesta³⁹, Y. Cui²⁶,
 F. Curciarello⁹⁶, D. Cussans¹⁹, J. Dai⁷⁶, O. Dalager⁶⁶, W. Dallaway¹⁹⁹,
 R. D'Amico^{95,67}, H. da Motta³³, Z. A. Dar²¹³, R. Darby¹⁹¹, L. Da Silva Peres⁶⁵,
 Q. David¹¹³, G. S. Davies¹⁴⁶, S. Davini⁹⁷, J. Dawson¹⁶², R. De Aguiar³⁰,
 P. Debbins¹¹¹, M. P. Decowski^{148,3}, A. de Gouvêa¹⁵², P. C. De Holanda³⁰, P. De
 Jong^{148,3}, P. Del Amo Sanchez⁵¹, G. De Lauretis¹¹³, A. Delbart³⁴,
 M. Delgado^{99,142}, A. Dell'Acqua³⁵, G. Delle Monache⁹⁶, N. Delmonte^{100,163}, P. De
 Lurgio⁸, G. De Matteis^{98,180}, J. R. T. de Mello Neto⁶⁵, A. P. A. De Mendonca³⁰,
 D. M. DeMuth²⁰⁶, S. Dennis²⁹, C. Densham¹⁷⁹, P. Denton²⁰, G. W. Deptuch²⁰,
 A. De Roeck³⁵, V. De Romeri⁸⁴, J. P. Detje²⁹, J. Devine³⁵, K. Dhanmeher¹¹³,
 R. Dharmapalan⁷⁹, M. Dias²⁰¹, A. Diaz²⁸, J. S. Diaz⁹², F. Diaz¹⁷⁰, F. Di
 Capua^{101,147}, A. Di Domenico^{182,105}, S. Di Domizio^{97,71}, S. Di Falco¹⁰⁴, L. Di
 Giulio³⁵, P. Ding⁶⁶, L. Di Noto^{97,71}, E. Diociaiuti⁹⁶, G. Di Sciascio¹⁰⁶, V. Di
 Silvestre¹⁸², C. Distefano¹⁰⁷, R. Di Stefano¹⁰⁶, R. Diurba¹⁴, M. Diwan²⁰,
 Z. Djurcic⁸, S. Dolan³⁵, M. Dolce²¹², M. J. Dolinski⁵⁴, D. Domenici⁹⁶,
 S. Dominguez³⁹, S. Donati^{104,168}, S. Doran¹¹², D. Douglas¹⁸⁵, T.A. Doyle¹⁸⁹,
 F. Drielsma¹⁸⁵, D. Duchesneau⁵¹, K. Duffy¹⁵⁷, K. Dugas²⁴, P. Dunne⁸⁹,
 B. Dutta¹⁹⁵, D. A. Dwyer¹²⁹, A. S. Dyshkant¹⁵¹, S. Dytman¹⁶⁹, M. Eads¹⁵¹,
 A. Earle¹⁹¹, S. Edayath¹¹², D. Edmunds¹⁴¹, J. Eisch⁶⁶, W. Emark¹⁵¹,
 P. Englezos¹⁷⁸, A. Ereditato³⁷, T. Erjavec²³, C. O. Escobar⁶⁶, J. J. Evans¹³⁷,

E. Ewart⁹², A. C. Ezeribe¹⁸⁴, K. Fahey⁶⁶, A. Falcone^{99,142}, M. Fani^{145,132},
 D. Faragher¹⁴⁵, C. Farnese¹⁰², Y. Farzan¹¹⁴, J. Felix⁷⁷, Y. Feng¹¹², M. Ferreira
 da Silva²⁰¹, G. Ferry¹⁶¹, E. Fialova⁵⁰, L. Fields¹⁵³, P. Filip⁴⁹, A. Filkins¹⁹²,
 F. Filthaut^{148,174}, G. Fiorillo^{101,147}, M. Fiorini^{95,67}, S. Fogarty⁴⁴, W. Foreman¹³²,
 J. Fowler⁵⁵, J. Franc⁵⁰, K. Francis¹⁵¹, D. Franco³⁷, J. Franklin⁵⁶, J. Freeman⁶⁶,
 J. Fried²⁰, A. Friedland¹⁸⁵, M. Fucci¹⁸⁹, S. Fuess⁶⁶, I. K. Furic⁶⁸, K. Furman¹⁷³,
 A. P. Furmanski¹⁴⁵, R. Gaba¹⁶⁰, A. Gabrielli^{93,17}, A. M Gago¹⁷⁰, F. Galizzi^{99,142},
 H. Gallagher²⁰⁰, M. Galli¹⁶², N. Gallice²⁰, V. Galymov¹¹³, E. Gamberini³⁵,
 T. Gamble¹⁸⁴, R. Gandhi⁷⁸, S. Ganguly⁶⁶, F. Gao²⁷, S. Gao²⁰, D. Garcia-
 Gamez⁷³, M. Á. García-Peris¹³⁷, F. Gardim⁶², S. Gardiner⁶⁶, A. Gartman⁵⁰,
 A. Gauch¹⁴, P. Gauzzi^{182,105}, S. Gazzana⁹⁶, G. Ge⁴⁵, N. Geffroy⁵¹, B. Gelli³⁰,
 S. Gent¹⁸⁸, L. Gerlach²⁰, A. Ghosh¹¹², T. Giammaria^{95,67}, D. Gibin^{159,102},
 I. Gil-Botella³⁹, A. Gioiosa¹⁰⁶, S. Giovannella⁹⁶, A. K. Giri⁹¹, V. Giusti¹⁰⁴,
 D. Gnani¹²⁹, O. Gogota¹²⁷, S. Gollapinni¹³², K. Gollwitzer⁶⁶, R. A. Gomes⁶³,
 L. S. Gomez Fajardo¹⁸³, D. Gonzalez-Diaz⁸⁵, J. Gonzalez-Santome³⁵,
 M. C. Goodman⁸, S. Goswami¹⁶⁷, C. Gotti⁹⁹, J. Goudeau¹³³, C. Grace¹²⁹,
 E. Gramellini¹³⁷, R. Gran¹⁴⁴, P. Granger³⁵, C. Grant¹⁸, D. R. Gratieri^{70,30},
 G. Grauso¹⁰¹, P. Green¹⁵⁷, S. Greenberg^{22,129}, W. C. Griffith¹⁹¹, A. Gruber¹⁹⁴,
 K. Grzelak²⁰⁹, L. Gu¹²⁸, W. Gu²⁰, V. Guarino⁸, M. Guarise^{95,67}, R. Guenette¹³⁷,
 M. Guerzoni⁹³, D. Guffanti^{99,142}, A. Guglielmi¹⁰², F. Y. Guo¹⁸⁹, A. Gupta⁸⁷,
 V. Gupta^{148,3}, G. Gurung¹⁹⁷, D. Gutierrez¹⁷¹, P. Guzowski¹³⁷, M. M. Guzzo³⁰,
 S. Gwon³⁸, A. Habig¹⁴⁴, L. Haegel¹¹³, R. Hafeji^{84,85}, L. Hagaman³⁷, A. Hahn⁶⁶,
 J. Hakenmüller⁵⁵, T. Hamernik⁶⁶, P. Hamilton⁸⁹, J. Hancock¹⁶, M. Handley²⁹,
 F. Happacher⁹⁶, B. Harris¹⁶⁵, D. A. Harris^{217,66}, L. Harris⁷⁹, A. L. Hart¹⁷³,
 J. Hartnell¹⁹¹, T. Hartnett¹⁷⁹, J. Harton⁴⁴, T. Hasegawa¹²⁵, C. M. Hasnip³⁵,
 K. Hassinin⁸¹, R. Hatcher⁶⁶, S. Hawkins¹⁴¹, J. Hays¹⁷³, M. He⁸¹, A. Heavey⁶⁶,
 K. M. Heeger²¹⁵, A. Heindel¹⁸⁹, J. Heise¹⁹⁰, P. Hellmuth¹³⁴, L. Henderson¹⁵⁶,
 J. Hernández⁸⁴, M. A. Hernandez Morquecho¹⁴⁵, K. Herner⁶⁶, V. Hewes⁴⁰,
 A. Higuera¹⁷⁵, A. Himmel⁶⁶, E. Hinkle³⁷, L.R. Hirsch¹⁹³, J. Ho⁵³, J. Hoefken
 Zink⁹³, J. Hoff⁶⁶, A. Holin¹⁷⁹, T. Holvey¹⁵⁷, C. Hong¹⁶², S. Horiuchi²⁰⁸,
 G. A. Horton-Smith¹²³, R. Hosokawa¹¹⁸, T. Houdy¹⁶¹, B. Howard^{217,66},
 R. Howell¹⁷⁶, I. Hristova¹⁷⁹, M. S. Hronek⁶⁶, H. Hua⁸⁹, J. Huang²³,
 R.G. Huang¹²⁹, X. Huang¹⁴⁶, Z. Hulcher¹⁸⁵, A. Hussain¹²³, G. Iles⁸⁹, N. Ilic¹⁹⁹,
 A. M. Iliescu⁹⁶, R. Illingworth⁶⁶, G. Ingratta²¹⁷, A. Ioannisian²¹⁶, M. Ismerio
 Oliveira⁶⁵, C.M. Jackson¹⁵⁸, A. Jacobi²⁴, V. Jain¹, E. James⁶⁶, W. Jang¹⁹⁷,
 B. Jargowsky²⁴, D. Jena⁶⁶, I. Jentz²¹⁴, C. Jiang¹¹⁹, J. Jiang¹⁸⁹, A. Jipa²¹,
 J. H. Jo²⁰, F. R. Joaquim^{130,116}, W. Johnson¹⁸⁷, C. Jollet¹³⁴, R. Jones¹⁸⁴,
 M. Joshi¹⁸⁶, N. Jovancevic¹⁵⁴, M. Judah¹⁶⁹, C. K. Jung¹⁸⁹, K. Y. Jung¹⁷⁶,
 T. Junk⁶⁶, Y. Jwa^{185,45}, M. Kabirnezhad⁸⁹, A. C. Kaboth^{177,179}, I. Kadenko¹²⁷,
 O. Kalikulov², D. Kalra⁴⁵, M. Kandemir⁶⁰, S. Kar¹⁹, G. Karagiorgi⁴⁵,
 G. Karaman¹¹¹, A. Karcher¹²⁹, Y. Karyotakis⁵¹, S. P. Kasetti¹³³, L. Kashur⁴⁴,
 A. Kauther¹⁵¹, N. Kazaryan²¹⁶, L. Ke²⁰, E. Kearns¹⁸, P.T. Keener¹⁶⁵,

K.J. Kelly¹⁹⁵, R. Keloth²⁰⁸, E. Kemp³⁰, O. Kemularia⁷², Y. Kermaidic¹⁶¹,
 W. Ketchum⁶⁶, S. H. Kettell²⁰, N. Khan⁸⁹, A. Khvedelidze⁷², D. Kim¹⁹⁵,
 J. Kim¹⁷⁶, M. J. Kim⁶⁶, S. Kim³⁸, B. King⁶⁶, M. King³⁷, M. Kirby²⁰,
 A. Kish⁶⁶, J. Klein¹⁶⁵, J. Kleykamp¹⁴⁶, A. Klustova⁸⁹, T. Kobilarcik⁶⁶,
 L. Koch¹³⁶, K. Koehler²¹⁴, L. W. Koerner⁸¹, D. H. Koh¹⁸⁵, M. Kordosky²¹³,
 T. Kosc⁷⁶, V. A. Kostelecký⁹², I. Kotler⁵⁴, W. Krah¹⁴⁸, R. Kralik¹⁹¹,
 M. Kramer¹²⁹, F. Krennrich¹¹², T. Kroupova¹⁶⁵, S. Kubota¹²⁹, M. Kubu³⁵,
 V. A. Kudryavtsev¹⁸⁴, G. Kufatty⁶⁹, S. Kuhlmann⁸, A. Kumar¹⁴⁵, J. Kumar⁷⁹,
 M. Kumar⁸⁷, P. Kumar¹²⁰, P. Kumar¹⁸⁴, S. Kumaran²⁴, J. Kunzmann¹⁴,
 V. Kus⁵⁰, T. Kutter¹³³, J. Kvasnicka⁴⁹, T. Labree¹⁵¹, M. Lachat¹⁷⁶, T. Lackey⁶⁶,
 I. Lalău²¹, A. Lambert¹²⁹, B. J. Land¹⁶⁵, C. E. Lane⁵⁴, N. Lane¹³⁷, K. Lang¹⁹⁸,
 T. Langford²¹⁵, M. Langstaff¹³⁷, F. Lanni³⁵, J. Larkin¹⁷⁶, P. Lasorak⁸⁹,
 D. Last¹⁷⁶, A. Laundrie²¹⁴, G. Laurenti⁹³, E. Lavaut¹⁶¹, H. Lay¹²⁸, I. Lazanu²¹,
 R. LaZur⁴⁴, M. Lazzaroni^{100,143}, S. Leardini⁸⁵, J. Learned⁷⁹, T. LeCompte¹⁸⁵,
 G. Lehmann Miotto³⁵, R. Lehnert⁹², M. Leitner¹²⁹, H. Lemoine¹⁴⁴, D. Leon
 Silverio¹⁸⁷, L. M. Lepin⁶⁹, J.-Y Li⁵⁷, S. W. Li²⁴, Y. Li²⁰, R. Lima⁶², C. S. Lin¹²⁹,
 D. Lindebaum¹⁹, S. Linden²⁰, R. A. Lineros³², A. Lister²¹⁴, B. R. Littlejohn⁸⁸,
 J. Liu²⁴, Y. Liu³⁷, S. Lockwitz⁶⁶, I. Lomidze⁷², K. Long⁸⁹, J. Lopez⁶, I. López de
 Rego³⁹, N. López-March⁸⁴, J. M. LoSecco¹⁵³, A. Lozano Sanchez⁵⁴, X.-G. Lu²¹⁰,
 K.B. Luk^{80,129,22}, X. Luo²⁷, E. Luppi^{95,67}, A. A. Machado³⁰, P. Machado⁶⁶,
 C. T. Macias⁹², J. R. Macier⁶⁶, M. MacMahon²⁰³, S. Magill⁸, C. Magueur¹⁶¹,
 K. Mahn¹⁴¹, A. Maio^{130,61}, N. Majeed¹²³, A. Major⁵⁵, K. Majumdar¹³¹,
 A. Malige⁴⁵, S. Mameli¹⁰⁴, M. Man¹⁹⁹, R. C. Mandujano²⁴, J. Maneira^{130,61},
 S. Manly¹⁷⁶, K. Manolopoulos¹⁷⁹, M. Manrique Plata⁹², S. Manthey Corchado³⁹,
 L. Manzanillas-Velez⁵¹, E. Mao¹⁹², M. Marchan⁶⁶, A. Marchionni⁶⁶,
 D. Marfatia⁷⁹, C. Mariani²⁰⁸, J. Maricic⁷⁹, F. Marinho¹¹⁷, A. D. Marino⁴³,
 T. Markiewicz¹⁸⁵, F. Das Chagas Marques³⁰, M. Marshak¹⁴⁵, C. M. Marshall¹⁷⁶,
 J. Marshall²¹⁰, L. Martina^{98,180}, J. Martín-Albo⁸⁴, D.A. Martinez Caicedo¹⁸⁷,
 M. Martinez-Casales⁶⁶, F. Martínez López⁹², S. Martynenko²⁰, V. Mascagna⁹⁹,
 A. Mastbaum¹⁷⁸, M. Masud³⁸, F. Matichard¹²⁹, G. Matteucci^{101,147},
 J. Matthews¹³³, C. Mauger¹⁶⁵, N. Mauri^{93,17}, K. Mavrokordidis¹³¹, I. Mawby¹²⁸,
 F. Mayhew¹⁴¹, T. McAskill²¹¹, N. McConkey¹⁷³, B. McConnell⁹²,
 K. S. McFarland¹⁷⁶, C. McGivern⁶⁶, C. McGrew¹⁸⁹, A. McNab¹³⁷, C. McNulty¹²⁹,
 J. Mead¹⁴⁸, L. Meazza⁹⁹, V. C. N. Meddage⁶⁸, A. Medhi⁹⁰, M. Mehmood²¹⁷,
 B. Mehta¹⁶⁰, P. Mehta¹²⁰, F. Mei^{93,17}, P. Melas¹¹, L. Mellet¹⁴¹, T. C. D. Melo⁶²,
 O. Mena⁸⁴, H. Mendez¹⁷¹, D. P. Méndez²⁰, A. Menegolli^{103,164}, G. Meng¹⁰²,
 A. C. E. A. Mercuri¹⁹³, A. Meregaglia¹³⁴, M. D. Messier⁹², S. Metallo¹⁴⁵,
 W. Metcalf¹³³, M. Mewes⁹², H. Meyer²¹², T. Miao⁶⁶, J. Micallef^{200,138},
 A. Miccoli⁹⁸, G. Michna¹⁸⁸, R. Milincic⁷⁹, F. Miller²¹⁴, G. Miller¹³⁷, W. Miller¹⁴⁵,
 A. Minotti^{99,142}, L. Miralles Verge³⁵, C. Mironov¹⁶², S. Miscetti⁹⁶, C. S. Mishra⁶⁶,
 P. Mishra⁸², S. R. Mishra¹⁸⁶, D. Mladenov³⁵, I. Mocioiu¹⁶⁶, A. Mogan⁶⁶,
 R. Mohanta⁸², T. A. Mohayai⁹², N. Mokhov⁶⁶, J. Molina¹⁰, L. Molina Bueno⁸⁴,

E. Montagna^{93,17}, A. Montanari⁹³, C. Montanari^{103,66,164}, D. Montanari⁶⁶,
 D. Montanino^{98,180}, L. M. Montaño Zetina⁴¹, M. Mooney⁴⁴, A. F. Moor¹⁸⁴,
 M. Moore¹⁸⁵, Z. Moore¹⁹², D. Moreno⁷, G. Moreno-Granados²⁰⁸, O. Moreno-
 Palacios²¹³, L. Morescalchi¹⁰⁴, C. Morris⁸¹, E. Motuk²⁰³, C. A. Moura⁶⁴,
 G. Mouster¹²⁸, W. Mu⁶⁶, L. Mualem²⁸, J. Mueller⁶⁶, M. Muether²¹²,
 F. Muheim⁵⁷, A. Muir⁵², Y. Mukhamejanov², A. Mukhamejanova²,
 M. Mulhearn²³, D. Munford⁸¹, L. J. Munteanu³⁵, H. Muramatsu¹⁴⁵, J. Muraz⁷⁶,
 M. Murphy²⁰⁸, T. Murphy⁶⁶, A. Mytilinaki¹⁷⁹, J. Nachtman¹¹¹, Y. Nagai⁵⁹,
 S. Nagu¹³⁵, H. Nam³⁸, D. Naples¹⁶⁹, S. Narita¹¹⁸, J. Nava^{93,17}, A. Navrer-
 Agasson⁸⁹, N. Nayak²⁰, M. Nebot-Guinot⁵⁷, A. Nehm¹³⁶, J. K. Nelson²¹³,
 O. Neogi¹¹¹, J. Nesbit²¹⁴, M. Nessi^{66,35}, D. Newbold¹⁷⁹, M. Newcomer¹⁶⁵,
 D. Newmark¹³⁸, R. Nichol²⁰³, F. Nicolas-Arnaldos⁷³, A. Nielsen²⁴, A. Nikolica¹⁶⁵,
 J. Nikolov¹⁵⁴, E. Niner⁶⁶, X. Ning²⁰, K. Nishimura⁷⁹, A. Norman⁶⁶,
 A. Norrick⁶⁶, F. Noto¹⁰⁷, P. Novella⁸⁴, A. Nowak¹²⁸, J. A. Nowak¹²⁸,
 M. Oberling⁸, J. P. Ochoa-Ricoux²⁴, S. Oh⁵⁵, S.B. Oh⁶⁶, A. Olivier⁸, T. Olson⁸¹,
 Y. Onel¹¹¹, Y. Onishchuk¹²⁷, A. Oranday⁹², M. Osbiston²¹⁰, J. A. Osorio Vélez⁶,
 L. O'Sullivan¹³⁶, L. Otiniano Ormachea^{46,109}, L. Pagani²³, G. Palacio⁵⁸,
 O. Palamara⁶⁶, S. Palestini¹⁰⁸, J. M. Paley⁶⁶, M. Pallavicini^{97,71}, C. Palomares³⁹,
 S. Pan¹⁶⁷, M. Panareo^{98,180}, P. Panda⁸², V. Pandey⁶⁶, W. Panduro Vazquez¹⁷⁷,
 E. Pantic²³, V. Paolone¹⁶⁹, A. Papadopoulou¹³², R. Papaleo¹⁰⁷, D. Papoulias¹¹,
 S. Paramesvaran¹⁹, J. Park¹⁴⁵, J. Park³⁸, S. Parke⁶⁶, S. Parsa¹⁴, S. Parveen¹²⁰,
 M. Parvu²¹, D. Pasciuto¹⁰⁴, S. Pascoli^{93,17}, L. Pasqualini^{93,17}, J. Pasternak⁸⁹,
 G. Patel¹⁴⁵, J. L. Paton⁶⁶, C. Patrick⁵⁷, L. Patrizii⁹³, R. B. Patterson²⁸,
 T. Patzak¹⁶², A. Paudel⁶⁶, J. Paul¹⁴⁸, L. Paulucci¹¹⁷, Z. Pavlovic⁶⁶,
 G. Pawloski¹⁴⁵, D. Payne¹³¹, A. Peake¹⁷⁷, V. Pec⁴⁹, E. Pedreschi¹⁰⁴,
 S. J. M. Peeters¹⁹¹, W. Pellico⁶⁶, E. Pennacchio¹¹³, A. Penzo¹¹¹,
 O. L. G. Peres³⁰, Y. F. Perez Gonzalez⁵⁶, L. Pérez-Molina³⁹, C. Pernas²¹³,
 J. Perry⁵⁷, D. Pershey⁶⁹, G. Pessina⁹⁹, G. Petrillo¹⁸⁵, C. Petta^{94,31}, R. Petti¹⁸⁶,
 M. Pfaff⁸⁹, V. Pia^{93,17}, G. M. Piacentino¹⁰⁶, L. Pickering^{179,177}, L. Pierini^{67,95},
 F. Pietropaolo^{35,102}, V.L.Pimentel^{47,30}, G. Pinaroli²⁰, S. Pincha⁹⁰,
 J. Pinchault⁵¹, K. Pitts²⁰⁸, P. Plesniak⁸⁹, K. Pletcher¹⁴¹, K. Plows¹⁵⁷,
 C. Pollack¹⁷¹, T. Pollmann^{148,3}, F. Pompa⁸⁴, X. Pons³⁵, N. Poonthottathil^{87,112},
 V. Popov¹⁹⁴, F. Poppi^{93,17}, J. Porter¹⁹¹, L. G. Porto Paixão³⁰, M. Potekhin²⁰,
 M. Pozzato^{93,17}, R. Pradhan⁹¹, T. Prakash¹²⁹, M. Prest⁹⁹, F. Psihas⁶⁶,
 D. Pugnere¹¹³, D. Pullia^{35,162}, X. Qian²⁰, J. Queen⁵⁵, J. L. Raaf⁶⁶,
 M. Rabelhofer⁹², V. Radeka²⁰, J. Rademacker¹⁹, F. Raffaelli¹⁰⁴, A. Rafique⁸,
 U. Rahaman¹⁹⁹, A. Rahe¹⁵¹, S. Rajagopalan²⁰, M. Rajaoalisoa⁴⁰, I. Rakhno⁶⁶,
 L. Rakotondravohitra⁵, M. A. Ralaikoto⁵, L. Ralte⁹¹, M. A. Ramirez Delgado¹⁶⁵,
 B. Ramson⁶⁶, S. S. Randriamanampisoa⁵, A. Rappoldi^{103,164}, G. Raselli^{103,164},
 T. Rath¹⁸⁷, P. Ratoff¹²⁸, R. Ray⁶⁶, H. Razafinime⁴⁰, R. F. Razakamiandra¹⁸⁹,
 E. M. Rea¹⁴⁵, J. S. Real⁷⁶, B. Rebel^{214,66}, R. Rechenmacher⁶⁶,
 J. Reichenbacher¹⁸⁷, S. D. Reitzner⁶⁶, E. Renner¹³², S. Repetto^{97,71}, S. Rescia²⁰,

F. Resnati³⁵, C. Reynolds¹⁷³, M. Ribas¹⁹³, S. Riboldi¹⁰⁰, C. Riccio¹⁸⁹,
 G. Riccobene¹⁰⁷, J. S. Ricol⁷⁶, M. Rigan¹⁹¹, A. Rikalo¹⁵⁴, E. V. Rincón⁵⁸,
 A. Ritchie-Yates¹⁷⁷, D. Rivera¹³², A. Robert⁷⁶, A. Roberts¹³¹, E. Robles²⁴,
 A. Roche⁸⁴, M. Roda¹³¹, D. Rodas Rodríguez⁸⁵, M. J. O. Rodrigues⁶²,
 J. Rodriguez Rondon¹⁸⁷, S. Rosauro-Alcaraz¹⁶¹, P. Rosier¹⁶¹, D. Ross¹⁴¹,
 M. Rossella^{103,164}, M. Ross-Lonergan⁴⁵, T. Rotsy⁵, N. Roy²¹⁷, P. Roy²¹²,
 P. Roy²⁰⁸, C. Rubbia⁷⁴, D. Rudik¹⁰¹, A. Ruggeri⁹³, G. Ruiz Ferreira¹³⁷,
 K. Rushiya¹²⁰, B. Russell¹³⁸, S. Sacerdoti¹⁶², N. Saduyev², S. Saha¹⁶⁹,
 S. K. Sahoo⁹¹, N. Sahu⁹¹, S. Sakhiyev², P. Sala⁶⁶, G. Salmoria¹⁹³, S. Samanta⁹⁷,
 M. C. Sanchez⁶⁹, A. Sánchez-Castillo⁷³, P. Sanchez-Lucas⁷³, D. A. Sanders¹⁴⁶,
 S. Sanfilippo¹⁰⁷, D. Santoro^{100,163}, N. Saoulidou¹¹, P. Sapienza¹⁰⁷, I. Sarcevic⁹,
 I. Sarra⁹⁶, G. Savage⁶⁶, V. Savinov¹⁶⁹, G. Scanavini²¹⁵, A. Scanu⁹⁹,
 A. Scaramelli¹⁰³, T. Schefke¹³³, H. Schellman^{156,66}, S. Schifano^{95,67},
 P. Schlabach⁶⁶, D. Schmitz³⁷, A. W. Schneider¹³⁸, K. Scholberg⁵⁵,
 A. Schroeder¹⁴⁵, A. Schukraft⁶⁶, B. Schuld⁴³, S. Schwartz²⁸, A. Segade²⁰⁷,
 H. Segal¹⁹⁴, E. Segreto³⁰, A. Selyunin¹⁴, D. Senadheera¹⁶⁹, C. R. Senise²⁰¹,
 J. Sensenig¹⁶⁵, S.H. Seo⁶⁶, D. Seppela¹⁴¹, M. H. Shaevitz⁴⁵, P. Shanahan⁶⁶,
 P. Sharma¹⁶⁰, R. Kumar¹⁷², S. Sharma Poudel¹⁸⁷, K. Shaw¹⁹¹, T. Shaw⁶⁶,
 K. Shchabلو¹¹³, J. Shen¹⁶⁵, C. Shepherd-Themistocleous¹⁷⁹, J. Shi²⁹, W. Shi¹⁸⁹,
 S. Shin¹²¹, S. Shivakoti²¹², A. Shmakov²⁴, I. Shoemaker²⁰⁸, D. Shooltz¹⁴¹,
 R. Shrock¹⁸⁹, M. Siden⁴⁴, J. Silber¹²⁹, L. Simard¹⁶¹, J. Sinclair¹⁸⁵, G. Sinev¹⁸⁷,
 Jaydip Singh²³, J. Singh¹³⁵, L. Singh⁴⁸, P. Singh¹⁷³, V. Singh⁴⁸, S. Singh
 Chauhan¹⁶⁰, R. Sipos³⁵, C. Sironneau¹⁶², G. Sirri⁹³, K. Siyeon³⁸, K. Skarpaas¹⁸⁵,
 J. Smedley¹⁷⁶, J. Smith¹⁸⁹, P. Smith⁹², J. Smolik^{50,49}, M. Smy²⁴, M. Snape²¹⁰,
 E. L. Snider⁶⁶, P. Snopok⁸⁸, M. Soares Nunes⁶⁶, H. Sobel²⁴, M. Soderberg¹⁹²,
 H. Sogarwal¹¹², C. J. Solano Salinas²⁰⁵, S. Söldner-Rembold⁸⁹, N. Solomey²¹²,
 V. Solovov¹³⁰, W. E. Sondheim¹³², M. Sorbara¹⁰⁶, M. Sorel⁸⁴, J. Soto-Oton⁸⁴,
 A. Sousa⁴⁰, K. Soustruznik³⁶, D. Souza Correia³³, F. Spinella¹⁰⁴, J. Spitz¹⁴⁰,
 N. J. C. Spooner¹⁸⁴, D. Stalder¹⁰, M. Stancari⁶⁶, L. Stanco^{159,102}, J. Steenis²³,
 R. Stein¹⁹, H. M. Steiner¹²⁹, A. F. Steklain Lisbôa¹⁹³, J. Stewart²⁰, B. Stillwell³⁷,
 J. Stock¹⁸⁷, T. Stokes²¹⁵, T. Strauss⁶⁶, L. Strigari¹⁹⁵, A. Stuart⁴², J. G. Suarez⁵⁸,
 J. Subash¹⁶, A. Surdo⁹⁸, L. Suter⁶⁶, A. Sutton⁶⁹, K. Sutton²⁸, Y. Suvorov^{101,147},
 R. Svoboda²³, S. K. Swain¹⁴⁹, C. Sweeney¹¹², B. Szczerbinska¹⁹⁶, A. M. Szelc⁵⁷,
 A. Sztuc²⁰³, A. Taffara¹⁰⁴, N. Talukdar¹⁸⁶, J. Tamara⁷, H. A. Tanaka¹⁸⁵,
 S. Tang²⁰, N. Taniuchi²⁹, A. M. Tapia Casanova¹³⁹, A. Tapper⁸⁹, S. Tariq⁶⁶,
 E. Tatar⁸³, R. Tayloe⁹², A. M. Teklu¹⁸⁹, K. Tellez Giron Flores²⁰, J. Tena
 Vidal¹⁹⁴, P. Tennessen^{129,4}, M. Tenti⁹³, K. Terao¹⁸⁵, F. Terranova^{99,142},
 G. Testera⁹⁷, T. Thakore⁴⁰, A. Thea¹⁷⁹, S. Thomas¹⁹², A. Thompson¹⁵²,
 C. Thorpe¹³⁷, S. C. Timm⁶⁶, E. Tiras^{60,111}, V. Tishchenko²⁰, S. Tiwari¹⁷⁶,
 N. Todorović¹⁵⁴, L. Tomassetti^{95,67}, A. Tonazzo¹⁶², D. Torbunov²⁰, D. Torres
 Muñoz¹⁸⁷, M. Torti^{99,142}, M. Tortola⁸⁴, Y. Torun⁸⁸, N. Tosi⁹³, D. Totani⁴⁴,
 M. Toups⁶⁶, C. Touramanis¹³¹, V. Trabattoni¹⁰⁰, D. Tran⁸¹, J. Trevor²⁸,

E. Triller¹⁴¹, S. Trilov¹⁹, D. Trotta⁹⁹, J. Truchon²¹⁴, D. Truncali^{182,105},
 W. H. Trzaska¹²², Y. Tsai²⁴, Y.-T. Tsai¹⁸⁵, Z. Tsamalaidze⁷², K. V. Tsang¹⁸⁵,
 N. Tsverava⁷², S. Z. Tu¹¹⁹, S. Tufanli³⁵, C. Tunnell¹⁷⁵, S. Turnberg⁸⁸,
 J. Turner⁵⁶, M. Tuzi⁸⁴, M. Tzanov¹³³, M. A. Uchida²⁹, J. Ureña González⁸⁴,
 J. Urheim⁹², T. Usher¹⁸⁵, H. Utaegbulam¹⁷⁶, S. Uzunyan¹⁵¹, M. R. Vagins^{124,24},
 P. Vahle²¹³, G. A. Valdivieso⁶², E. Valencia⁷⁷, R. Valentim²⁰¹, Z. Vallari¹⁵⁵,
 E. Vallazza⁹⁹, J. W. F. Valle⁸⁴, R. Van Berg¹⁶⁵, D. V. Forero¹³⁹, P. Van
 Gemmeren⁸, A. Vannozzi⁹⁶, M. Van Nuland-Troost¹⁴⁸, F. Varanini¹⁰², D. Vargas
 Oliva¹⁹⁹, N. Vaughan¹⁵⁶, K. Vaziri⁶⁶, A. Vázquez-Ramos⁷³, J. Vega⁴⁶,
 J. Vences^{130,61}, S. Ventura¹⁰², A. Verdugo³⁹, M. Verzocchi⁶⁶, K. Vetter⁶⁶,
 M. Vicenzi²⁰, H. Vieira de Souza¹⁶², C. Vignoli⁷⁵, C. Vilela¹³⁰, E. Villa³⁵,
 S. Viola¹⁰⁷, B. Viren²⁰, G. V. Stenico⁵⁷, R. Vizarreta¹⁷⁶, A. P. Vizcaya
 Hernandez⁴⁴, S. Vlachos¹³⁷, G. Vorobyev¹⁸⁶, Q. Vuong¹⁷⁶, A. V. Waldron¹⁷³,
 L. Walker⁸¹, H. Wallace¹⁷⁷, M. Wallach¹⁴¹, J. Walsh¹⁴¹, T. Walton⁶⁶, L. Wan⁶⁶,
 B. Wang¹¹¹, H. Wang²⁵, J. Wang¹⁸⁷, M.H.L.S. Wang⁶⁶, X. Wang⁶⁶, Y. Wang⁸⁶,
 D. Warner⁴⁴, L. Warsame¹⁷⁹, M.O. Wascko^{157,179}, D. Waters²⁰³, A. Watson¹⁶,
 K. Wawrowska^{179,191}, A. Weber^{136,66}, C. M. Weber¹⁴⁵, M. Weber¹⁴, H. Wei¹³³,
 A. Weinstein¹¹², S. Westerdale²⁶, M. Wetstein¹¹², K. Whalen¹⁷⁹, A.J. White²¹⁵,
 L. H. Whitehead²⁹, D. Whittington¹⁹², F. Wieler¹⁹³, J. Wilhelmi²¹⁵,
 M. J. Wilking¹⁴⁵, A. Wilkinson²¹⁰, C. Wilkinson¹²⁹, F. Wilson¹⁷⁹,
 R. J. Wilson⁴⁴, P. Winter⁸, J. Wolcott²⁰⁰, J. Wolfs¹⁷⁶, T. Wongjirad²⁰⁰,
 A. Wood⁸¹, K. Wood¹²⁹, D. Wooley¹³², E. Worcester²⁰, M. Worcester²⁰,
 K. Wresilo²⁹, M. Wright¹³⁷, M. Wrobel⁴⁴, S. Wu¹⁴⁵, W. Wu²⁴, Z. Wu²⁴,
 M. Wurm¹³⁶, J. Wyenberg⁵³, B. M. Wynne⁵⁷, Y. Xiao²⁴, I. Xiotidis⁸⁹,
 B. Yaeggy⁴⁰, N. Yahlali⁸⁴, E. Yandel²⁷, G. Yang^{20,189}, J. Yang⁸⁰, T. Yang⁶⁶,
 A. Yankelevich²⁴, L. Yates⁶⁶, U. (Yevarouskaya¹⁸⁹, K. Yonehara⁶⁶, T. Young¹⁵⁰,
 B. Yu²⁰, H. Yu²⁰, J. Yu¹⁹⁷, W. Yuan⁵⁷, M. Zabloudil⁵⁰, R. Zaki²¹⁷,
 J. Zalesak⁴⁹, L. Zambelli⁵¹, B. Zamorano⁷³, A. Zani¹⁰⁰, O. Zapata⁶,
 L. Zazueta¹⁹², G. P. Zeller⁶⁶, J. Zennamo⁶⁶, J. Zettlemoyer⁶⁶, K. Zeug²¹⁴,
 C. Zhang²⁰, S. Zhang⁹², Y. Zhang²⁰, L. Zhao²⁴, M. Zhao²⁰, E. D. Zimmerman⁴³,
 S. Zucchelli^{93,17}, A. Zummo¹⁷⁸, V. Zutshi¹⁵¹, R. Zwaska⁶⁶

¹University of Albany, SUNY, Albany, NY 12222, USA.

²Institute of Nuclear Physics at Almaty, Almaty 050032, Kazakhstan .

³University of Amsterdam, NL-1098 XG Amsterdam, The Netherlands.

⁴Antalya Bilim University, 07190 Döşemealtı/Antalya, Turkey.

⁵University of Antananarivo, Antananarivo 101, Madagascar.

⁶University of Antioquia, Medellín, Colombia.

⁷Universidad Antonio Nariño, Bogotá, Colombia.

⁸Argonne National Laboratory, Argonne, IL 60439, USA.

⁹University of Arizona, Tucson, AZ 85721, USA.

¹⁰Universidad Nacional de Asunción, San Lorenzo, Paraguay.

¹¹University of Athens, Zografou GR 157 84, Greece.

¹²Universidad del Atlántico, Barranquilla, Atlántico, Colombia.

¹³Augustana University, Sioux Falls, SD 57197, USA.
¹⁴University of Bern, CH-3012 Bern, Switzerland.
¹⁵Beykent University, Istanbul, Turkey.
¹⁶University of Birmingham, Birmingham B15 2TT, United Kingdom.
¹⁷Università di Bologna, 40127 Bologna, Italy.
¹⁸Boston University, Boston, MA 02215, USA.
¹⁹University of Bristol, Bristol BS8 1TL, United Kingdom.
²⁰Brookhaven National Laboratory, Upton, NY 11973, USA.
²¹University of Bucharest, Bucharest, Romania.
²²University of California Berkeley, Berkeley, CA 94720, USA.
²³University of California Davis, Davis, CA 95616, USA.
²⁴University of California Irvine, Irvine, CA 92697, USA.
²⁵University of California Los Angeles, Los Angeles, CA 90095, USA.
²⁶University of California Riverside, Riverside CA 92521, USA.
²⁷University of California Santa Barbara, Santa Barbara, CA 93106, USA.
²⁸California Institute of Technology, Pasadena, CA 91125, USA.
²⁹University of Cambridge, Cambridge CB3 0HE, United Kingdom.
³⁰Universidade Estadual de Campinas, Campinas - SP, 13083-970, Brazil.
³¹Università di Catania, 2 - 95131 Catania, Italy.
³²Universidad Católica del Norte, Antofagasta, Chile.
³³Centro Brasileiro de Pesquisas Físicas, Rio de Janeiro, RJ 22290-180, Brazil.
³⁴IRFU, CEA, Université Paris-Saclay, F-91191 Gif-sur-Yvette, France.
³⁵CERN, The European Organization for Nuclear Research, 1211 Meyrin, Switzerland.
³⁶Institute of Particle and Nuclear Physics of the Faculty of Mathematics and Physics of the Charles University, 180 00 Prague 8, Czech Republic .
³⁷University of Chicago, Chicago, IL 60637, USA.
³⁸Chung-Ang University, Seoul 06974, South Korea.
³⁹CIEMAT, Centro de Investigaciones Energéticas, Medioambientales y Tecnológicas, E-28040 Madrid, Spain.
⁴⁰University of Cincinnati, Cincinnati, OH 45221, USA.
⁴¹Centro de Investigación y de Estudios Avanzados del Instituto Politécnico Nacional (Cinvestav), Mexico City, Mexico.
⁴²Universidad de Colima, Colima, Mexico.
⁴³University of Colorado Boulder, Boulder, CO 80309, USA.
⁴⁴Colorado State University, Fort Collins, CO 80523, USA.
⁴⁵Columbia University, New York, NY 10027, USA.
⁴⁶Comisión Nacional de Investigación y Desarrollo Aeroespacial, Lima, Peru.
⁴⁷Centro de Tecnología da Informação Renato Archer, Amarais - Campinas, SP - CEP 13069-901.
⁴⁸Central University of South Bihar, Gaya, 824236, India .
⁴⁹Institute of Physics, Czech Academy of Sciences, 182 00 Prague 8, Czech Republic.
⁵⁰Czech Technical University, 115 19 Prague 1, Czech Republic.
⁵¹Laboratoire d'Annecy de Physique des Particules, Université Savoie Mont Blanc, CNRS, LAPP-IN2P3, 74000 Annecy, France.
⁵²Daresbury Laboratory, Cheshire WA4 4AD, United Kingdom.

⁵³Dordt University, Sioux Center, IA 51250, USA.
⁵⁴Drexel University, Philadelphia, PA 19104, USA.
⁵⁵Duke University, Durham, NC 27708, USA.
⁵⁶Durham University, Durham DH1 3LE, United Kingdom.
⁵⁷University of Edinburgh, Edinburgh EH8 9YL, United Kingdom.
⁵⁸Universidad EIA, Envigado, Antioquia, Colombia.
⁵⁹Eötvös Loránd University, 1053 Budapest, Hungary.
⁶⁰Erciyes University, Kayseri, Turkey.
⁶¹Faculdade de Ciências da Universidade de Lisboa - FCUL, 1749-016 Lisboa, Portugal.
⁶²Universidade Federal de Alfenas, Poços de Caldas - MG, 37715-400, Brazil.
⁶³Universidade Federal de Goias, Goiania, GO 74690-900, Brazil.
⁶⁴Universidade Federal do ABC, Santo André - SP, 09210-580, Brazil.
⁶⁵Universidade Federal do Rio de Janeiro, Rio de Janeiro - RJ, 21941-901, Brazil.
⁶⁶Fermi National Accelerator Laboratory, Batavia, IL 60510, USA.
⁶⁷University of Ferrara, Ferrara, Italy.
⁶⁸University of Florida, Gainesville, FL 32611-8440, USA.
⁶⁹Florida State University, Tallahassee, FL, 32306 USA.
⁷⁰Fluminense Federal University, 9 Icaraí Niterói - RJ, 24220-900, Brazil .
⁷¹Università degli Studi di Genova, Genova, Italy.
⁷²Georgian Technical University, Tbilisi, Georgia.
⁷³University of Granada & CAFPE, 18002 Granada, Spain.
⁷⁴Gran Sasso Science Institute, L'Aquila, Italy.
⁷⁵Laboratori Nazionali del Gran Sasso, L'Aquila AQ, Italy.
⁷⁶University Grenoble Alpes, CNRS, Grenoble INP, LPSC-IN2P3, 38000 Grenoble, France.
⁷⁷Universidad de Guanajuato, Guanajuato, C.P. 37000, Mexico.
⁷⁸Harish-Chandra Research Institute, Jhunsi, Allahabad 211 019, India.
⁷⁹University of Hawaii, Honolulu, HI 96822, USA.
⁸⁰Hong Kong University of Science and Technology, Kowloon, Hong Kong, China.
⁸¹University of Houston, Houston, TX 77204, USA.
⁸²University of Hyderabad, Gachibowli, Hyderabad - 500 046, India.
⁸³Idaho State University, Pocatello, ID 83209, USA.
⁸⁴Instituto de Física Corpuscular, CSIC and Universitat de València, 46980 Paterna, Valencia, Spain.
⁸⁵Instituto Galego de Física de Altas Enerxías, University of Santiago de Compostela, Santiago de Compostela, 15782, Spain.
⁸⁶Institute of High Energy Physics, Chinese Academy of Sciences, Beijing, China.
⁸⁷Indian Institute of Technology Kanpur, Uttar Pradesh 208016, India.
⁸⁸Illinois Institute of Technology, Chicago, IL 60616, USA.
⁸⁹Imperial College of Science, Technology and Medicine, London SW7 2BZ, United Kingdom.
⁹⁰Indian Institute of Technology Guwahati, Guwahati, 781 039, India.
⁹¹Indian Institute of Technology Hyderabad, Hyderabad, 502285, India.
⁹²Indiana University, Bloomington, IN 47405, USA.
⁹³Istituto Nazionale di Fisica Nucleare Sezione di Bologna, 40127 Bologna BO, Italy.

⁹⁴Istituto Nazionale di Fisica Nucleare Sezione di Catania, I-95123 Catania, Italy.

⁹⁵Istituto Nazionale di Fisica Nucleare Sezione di Ferrara, I-44122 Ferrara, Italy.

⁹⁶Istituto Nazionale di Fisica Nucleare Laboratori Nazionali di Frascati, Frascati, Roma, Italy.

⁹⁷Istituto Nazionale di Fisica Nucleare Sezione di Genova, 16146 Genova GE, Italy.

⁹⁸Istituto Nazionale di Fisica Nucleare Sezione di Lecce, 73100 - Lecce, Italy.

⁹⁹Istituto Nazionale di Fisica Nucleare Sezione di Milano Bicocca, 3 - I-20126 Milano, Italy.

¹⁰⁰Istituto Nazionale di Fisica Nucleare Sezione di Milano, 20133 Milano, Italy.

¹⁰¹Istituto Nazionale di Fisica Nucleare Sezione di Napoli, I-80126 Napoli, Italy.

¹⁰²Istituto Nazionale di Fisica Nucleare Sezione di Padova, 35131 Padova, Italy.

¹⁰³Istituto Nazionale di Fisica Nucleare Sezione di Pavia, I-27100 Pavia, Italy.

¹⁰⁴Istituto Nazionale di Fisica Nucleare Laboratori Nazionali di Pisa, Pisa PI, Italy.

¹⁰⁵Istituto Nazionale di Fisica Nucleare Sezione di Roma, 00185 Roma RM, Italy.

¹⁰⁶Istituto Nazionale di Fisica Nucleare Roma Tor Vergata , 00133 Roma RM, Italy.

¹⁰⁷Istituto Nazionale di Fisica Nucleare Laboratori Nazionali del Sud, 95123 Catania, Italy.

¹⁰⁸Istituto Nazionale di Fisica Nucleare, Sezione di Torino, Turin, Italy.

¹⁰⁹Universidad Nacional de Ingeniería, Lima 25, Perú.

¹¹⁰University of Insubria, Via Ravasi, 2, 21100 Varese VA, Italy.

¹¹¹University of Iowa, Iowa City, IA 52242, USA.

¹¹²Iowa State University, Ames, Iowa 50011, USA.

¹¹³Institut de Physique des 2 Infinis de Lyon, 69622 Villeurbanne, France.

¹¹⁴Institute for Research in Fundamental Sciences, Tehran, Iran.

¹¹⁵Particle Physics and Cosmology International Research Laboratory , Chicago IL, 60637 USA.

¹¹⁶Instituto Superior Técnico - IST, Universidade de Lisboa, 1049-001 Lisboa, Portugal.

¹¹⁷Instituto Tecnológico de Aeronáutica, Sao Jose dos Campos, Brazil.

¹¹⁸Iwate University, Morioka, Iwate 020-8551, Japan.

¹¹⁹Jackson State University, Jackson, MS 39217, USA.

¹²⁰Jawaharlal Nehru University, New Delhi 110067, India.

¹²¹Jeonbuk National University, Jeonrabuk-do 54896, South Korea.

¹²²Jyväskylä University, FI-40014 Jyväskylä, Finland.

¹²³Kansas State University, Manhattan, KS 66506, USA.

¹²⁴Kavli Institute for the Physics and Mathematics of the Universe, Kashiwa, Chiba 277-8583, Japan.

¹²⁵High Energy Accelerator Research Organization (KEK), Ibaraki, 305-0801, Japan.

¹²⁶Korea Institute of Science and Technology Information, Daejeon, 34141, South Korea.

¹²⁷Taras Shevchenko National University of Kyiv, 01601 Kyiv, Ukraine.

¹²⁸Lancaster University, Lancaster LA1 4YB, United Kingdom.

¹²⁹Lawrence Berkeley National Laboratory, Berkeley, CA 94720, USA.

¹³⁰Laboratório de Instrumentação e Física Experimental de Partículas, 1649-003 Lisboa and 3004-516 Coimbra, Portugal.

¹³¹University of Liverpool, L69 7ZE, Liverpool, United Kingdom.

¹³²Los Alamos National Laboratory, Los Alamos, NM 87545, USA.

¹³³Louisiana State University, Baton Rouge, LA 70803, USA.

¹³⁴Laboratoire de Physique des Deux Infinis Bordeaux - IN2P3, F-33175 Gradignan, Bordeaux, France, .

¹³⁵University of Lucknow, Uttar Pradesh 226007, India.

¹³⁶Johannes Gutenberg-Universität Mainz, 55122 Mainz, Germany.

¹³⁷University of Manchester, Manchester M13 9PL, United Kingdom.

¹³⁸Massachusetts Institute of Technology, Cambridge, MA 02139, USA.

¹³⁹University of Medellín, Medellín, 050026 Colombia .

¹⁴⁰University of Michigan, Ann Arbor, MI 48109, USA.

¹⁴¹Michigan State University, East Lansing, MI 48824, USA.

¹⁴²Università di Milano Bicocca , 20126 Milano, Italy.

¹⁴³Università degli Studi di Milano, I-20133 Milano, Italy.

¹⁴⁴University of Minnesota Duluth, Duluth, MN 55812, USA.

¹⁴⁵University of Minnesota Twin Cities, Minneapolis, MN 55455, USA.

¹⁴⁶University of Mississippi, University, MS 38677 USA.

¹⁴⁷Università degli Studi di Napoli Federico II , 80138 Napoli NA, Italy.

¹⁴⁸Nikhef National Institute of Subatomic Physics, 1098 XG Amsterdam, Netherlands.

¹⁴⁹National Institute of Science Education and Research (NISER), Odisha 752050, India.

¹⁵⁰University of North Dakota, Grand Forks, ND 58202-8357, USA.

¹⁵¹Northern Illinois University, DeKalb, IL 60115, USA.

¹⁵²Northwestern University, Evanston, Il 60208, USA.

¹⁵³University of Notre Dame, Notre Dame, IN 46556, USA.

¹⁵⁴University of Novi Sad, 21102 Novi Sad, Serbia.

¹⁵⁵Ohio State University, Columbus, OH 43210, USA.

¹⁵⁶Oregon State University, Corvallis, OR 97331, USA.

¹⁵⁷University of Oxford, Oxford, OX1 3RH, United Kingdom.

¹⁵⁸Pacific Northwest National Laboratory, Richland, WA 99352, USA.

¹⁵⁹Università degli Studi di Padova, I-35131 Padova, Italy.

¹⁶⁰Panjab University, Chandigarh, 160014, India.

¹⁶¹Université Paris-Saclay, CNRS/IN2P3, IJCLab, 91405 Orsay, France.

¹⁶²Université Paris Cité, CNRS, Astroparticule et Cosmologie, Paris, France.

¹⁶³University of Parma, 43121 Parma PR, Italy.

¹⁶⁴Università degli Studi di Pavia, 27100 Pavia PV, Italy.

¹⁶⁵University of Pennsylvania, Philadelphia, PA 19104, USA.

¹⁶⁶Pennsylvania State University, University Park, PA 16802, USA.

¹⁶⁷Physical Research Laboratory, Ahmedabad 380 009, India.

¹⁶⁸Università di Pisa, I-56127 Pisa, Italy.

¹⁶⁹University of Pittsburgh, Pittsburgh, PA 15260, USA.

¹⁷⁰Pontificia Universidad Católica del Perú, Lima, Perú.

¹⁷¹University of Puerto Rico, Mayaguez 00681, Puerto Rico, USA.

¹⁷²Punjab Agricultural University, Ludhiana 141004, India.

¹⁷³Queen Mary University of London, London E1 4NS, United Kingdom .

¹⁷⁴Radboud University, NL-6525 AJ Nijmegen, Netherlands.

¹⁷⁵Rice University, Houston, TX 77005, USA.

¹⁷⁶University of Rochester, Rochester, NY 14627, USA.

¹⁷⁷Royal Holloway College London, London, TW20 0EX, United Kingdom.
¹⁷⁸Rutgers University, Piscataway, NJ, 08854, USA.
¹⁷⁹STFC Rutherford Appleton Laboratory, Didcot OX11 0QX, United Kingdom.
¹⁸⁰Università del Salento, 73100 Lecce, Italy.
¹⁸¹Universidad del Magdalena, Santa Marta - Colombia.
¹⁸²Sapienza University of Rome, 00185 Roma RM, Italy.
¹⁸³Universidad Sergio Arboleda, 11022 Bogotá, Colombia.
¹⁸⁴University of Sheffield, Sheffield S3 7RH, United Kingdom.
¹⁸⁵SLAC National Accelerator Laboratory, Menlo Park, CA 94025, USA.
¹⁸⁶University of South Carolina, Columbia, SC 29208, USA.
¹⁸⁷South Dakota School of Mines and Technology, Rapid City, SD 57701, USA.
¹⁸⁸South Dakota State University, Brookings, SD 57007, USA.
¹⁸⁹Stony Brook University, SUNY, Stony Brook, NY 11794, USA.
¹⁹⁰Sanford Underground Research Facility, Lead, SD, 57754, USA.
¹⁹¹University of Sussex, Brighton, BN1 9RH, United Kingdom.
¹⁹²Syracuse University, Syracuse, NY 13244, USA.
¹⁹³Universidade Tecnológica Federal do Paraná, Curitiba, Brazil.
¹⁹⁴Tel Aviv University, Tel Aviv-Yafo, Israel.
¹⁹⁵Texas A&M University, College Station, Texas 77840.
¹⁹⁶Texas A&M University - Corpus Christi, Corpus Christi, TX 78412, USA.
¹⁹⁷University of Texas at Arlington, Arlington, TX 76019, USA.
¹⁹⁸University of Texas at Austin, Austin, TX 78712, USA.
¹⁹⁹University of Toronto, Toronto, Ontario M5S 1A1, Canada.
²⁰⁰Tufts University, Medford, MA 02155, USA.
²⁰¹Universidade Federal de São Paulo, 09913-030, São Paulo, Brazil.
²⁰²Ulsan National Institute of Science and Technology, Ulsan 689-798, South Korea.
²⁰³University College London, London, WC1E 6BT, United Kingdom.
²⁰⁴University of Kansas, Lawrence, KS 66045.
²⁰⁵Universidad Nacional Mayor de San Marcos, Lima, Peru.
²⁰⁶Valley City State University, Valley City, ND 58072, USA.
²⁰⁷University of Vigo, E- 36310 Vigo Spain.
²⁰⁸Virginia Tech, Blacksburg, VA 24060, USA.
²⁰⁹University of Warsaw, 02-093 Warsaw, Poland.
²¹⁰University of Warwick, Coventry CV4 7AL, United Kingdom.
²¹¹Wellesley College, Wellesley, MA 02481, USA.
²¹²Wichita State University, Wichita, KS 67260, USA.
²¹³William and Mary, Williamsburg, VA 23187, USA.
²¹⁴University of Wisconsin Madison, Madison, WI 53706, USA.
²¹⁵Yale University, New Haven, CT 06520, USA.
²¹⁶Yerevan Institute for Theoretical Physics and Modeling, Yerevan 0036, Armenia.
²¹⁷York University, Toronto M3J 1P3, Canada.

Abstract

This paper reports on the capabilities in reconstructing and identifying atmospheric neutrino interactions in one of the Deep Underground Neutrino Experiment’s (DUNE) far detector modules, a liquid argon time projection chamber (LArTPC) with horizontal drift (FD-HD) of ionization electrons. The reconstruction is based upon the workflow developed for DUNE’s long-baseline oscillation analysis, with some necessary machine-learning models’ retraining and the addition of features relevant only to atmospheric neutrinos such as the neutrino direction reconstruction. Where relevant, the impact of the detection of the charged particles of the hadronic system is emphasized, and comparisons are carried out between the case when lepton-only information is considered in the reconstruction (as is the case for many neutrino oscillation experiments), versus when all particles identified in the LArTPC were included. Three neutrino direction reconstruction methods have been developed and studied for the atmospheric analyses: using lepton-only information, using all reconstructed particles, and using only correlations from reconstructed hits. The results indicate that incorporating more than just lepton information significantly improves the resolution of both neutrino direction and energy reconstruction. The angle reconstruction algorithms developed in this work result in no strong dependence on particle direction for reconstruction efficiencies or neutrino flavor identification. This comprehensive review of the reconstruction of atmospheric neutrinos in DUNE’s FD-HD LArTPC is the first step towards developing a first neutrino oscillation sensitivity analysis, which will ready DUNE for its first measurements.

Contents

1	Introduction	14	4	Summary and discussions	35
2	Analysis setup	15	4.1	Vertex	35
2.1	Sample generation and reconstruction	15	4.2	Particle reconstruction	36
2.2	Vertex fiducialization and interaction containment	17	4.3	Neutrino energy reconstruction	37
3	Atmospheric neutrino event reconstruction	18	4.4	Neutrino direction reconstruction	38
3.1	Neutrino-interaction vertex finding	18	4.5	Neutrino flavor determination	38
3.2	Particle reconstruction	19	5	Conclusions	39
3.2.1	Efficiency, purity, and completeness	19	6	Acknowledgements	40
3.2.2	Particle identification method	21			
3.2.3	Direction reconstruction	22			
3.2.4	Energy reconstruction: muons	23			
3.2.5	Energy reconstruction: electrons	25			
3.2.6	Energy reconstruction: charged hadrons	25			
3.3	Neutrino energy reconstruction	27			
3.3.1	Electron (anti-)neutrinos	27			
3.3.2	Muon (anti-)neutrinos	28			
3.4	Neutrino direction reconstruction	28			
3.4.1	Method	28			
3.4.2	Results	31			
3.5	Neutrino flavor determination	33			

1 Introduction

The Deep Underground Neutrino Experiment (DUNE) is under construction in the U.S. [1]. Its near detector (ND) is to be located at Fermilab in Illinois near the high-intensity LBNF beam target generated from a megawatt-class proton accelerator, while its far detector (FD) is hosted at a distance (or baseline) $L \sim 1300$ km away and ~ 1.5 km underground at Sanford Underground Research Facility (SURF) in South Dakota. Together, the ND and FD will enable a broad exploration of neutrinos and the physics laws that govern them [2]. DUNE’s primary science mission is to test the three-flavor paradigm of neutrino physics, determine the unknown neutrino mass ordering, make precise measurement of neutrino mixing parameters and determine the degree of charge-parity violation in the lepton sector, a key ingredient in certain theories seeking to resolve the origin of the baryon abundance of the universe [3–7].

The success of this program are the massive time projection chamber (TPC) modules of the FD, filled with a fiducial mass of 40 kilotons of liquid argon (LAr) [8, 9]. These LArTPCs will enable neutrino interactions to be resolved with high precision through the processing and reconstruction of ionizing activity down to order-millimeter length scales. It is expected that the first two modules of the FD (filled with 17 kilotons of LAr each) will be installed and ready to collect data a few years before the LBNF beam comes online. This presents the opportunity to start the physics program using natural sources of neutrinos, in particular neutrinos from secondary decays of particles produced by cosmic ray interactions in Earth’s atmosphere, *i.e.*, atmospheric neutrinos.

DUNE has sensitivity to oscillation parameters determined using atmospheric neutrinos [2]. In particular, measurements of Δm_{32}^2 can be carried out [10] to address the unknown neutrino mass ordering, along with the θ_{23} mixing angle to resolve its octant degeneracy ambiguity [2], and finally, a complementary beam-independent measurement of the δ_{CP} charge parity violating phase using sub-GeV atmospheric neutrinos [11]. Moreover, with $\mathcal{O}(10^3)$ ν_e and ν_μ atmospheric interactions expected per year in each of the FD modules [2], and the significant energy overlap with beam neutrino interactions, a high-level

of complementarity is expected between measurements performed across both sources. The reconstruction capabilities of LArTPC technology allows for particle detection and identification beyond only leptons; with a deep underground location protecting the large mass FDs from cosmogenic backgrounds, it is expected that high quality, high statistics measurements of atmospheric neutrinos are possible in DUNE. This will open opportunities for beyond Standard Model (BSM) physics studies [12, 13], including sterile neutrino searches [14], non-standard interactions [15], and mass-varying neutrinos [16]. Critical interrogation and correlation of atmospheric neutrino and cosmogenic activities can also aid in precision background predictions relevant for baryon number violation and (boosted) dark matter searches in the DUNE FDs. Overall, it is expected for DUNE measurements to complement and advance the atmospheric neutrino program carried out by present (IceCube [17], KM3NeT [18], Super-Kamiokande [19], *etc.*) and future (Hyper-Kamiokande [20]) neutrino experiments.

In general, there are clear advantages in exploiting atmospheric neutrinos: i) they are available at all times; ii) the oscillated flux contains all flavors of neutrinos and antineutrinos; iii) their energy E_ν spans a wide range (0.1 – 100 GeV) corresponding to roughly five orders of magnitude in L/E_ν ($\sim 1 - 6 \times 10^5$ km/GeV), broadening the reach of a neutrino physics program (*e.g.*, the BSM studies); iv) they can serve to break beam-only oscillation degeneracies and increase overall sensitivities via a future joint analysis, or act as a cross check method of common reconstruction techniques utilizing the same detectors; and v) they can be used for commissioning of the detectors in preparation for the beam neutrinos. Compared to their beamline counterparts, atmospheric neutrinos bring some complications: i) their flux is not known to the precision expected for beam neutrinos, depending on theoretical modeling of data from other experiments; ii) their direction is not known, which makes it necessary for the neutrino reconstruction to be understood and optimized for all incident angles; iii) the oscillation baseline (*i.e.*, the distance from where they are produced to the detectors) and the Earth’s structure, which they pass through, is less precisely known and model

dependent, respectively; iv) their interaction time (t_0) in the detector is not known, and requires additional measurements to determine the time when the ionization electrons begin to drift; v) the reconstruction of their wide range of energies is highly challenging, as the interaction processes and associated topologies vary widely as a function of incident neutrino energy; and, finally, vi) it is harder to distinguish neutrino from antineutrino in the atmospheric flux, which in the case of the beam can be achieved by using magnet-focusing horns to sign-select the mesons generating the (anti)neutrino beam.

Neutrinos' energy, direction, and flavor are reconstructed indirectly in a detector by identifying and reconstructing the aftermath of its interaction with the active medium of the detector. The accuracy of a neutrino interaction reconstruction directly impacts associated physics measurements, which depend inherently upon how precisely the position of the neutrino interaction vertex is determined, and on how well the energy, direction, and particle identification (PID) reconstruction algorithms perform for all daughter particles stemming from this vertex. This paper focuses on the deployment and validation of a complete set of reconstruction tools for atmospheric neutrinos in DUNE, which is an important stepping stone for any future physics analysis. Here, the performance of reconstruction algorithms will be presented for atmospheric neutrinos with energies between 100 MeV and 10 GeV, using a simulated DUNE FD LArTPC module. The upper limit is guided by the containment boundaries imposed by the reduced detector geometry used for this study. Particle reconstruction efficiencies and resolutions are evaluated, and their energy and direction dependence is reported.

The paper is structured as follows. First, a description will be given for the detector simulation setup, the reconstruction software, and simulated data sample used. Then, reconstruction algorithms relevant for the neutrino vertex, angle, and energy reconstruction will be presented, with performance assessments. The particle reconstruction and tagging performance, as well as a neutrino flavor identification method will also be discussed. Finally, a summary of the overall neutrino interaction reconstruction performance will be given, with an overview of the most promising

future developments, and closing with a discussion of this status in context of other atmospheric neutrino detectors.

2 Analysis setup

2.1 Sample generation and reconstruction

The first two FD modules that will start taking data will both be LArTPCs [1]. However, their design differs, with most changes stemming from the choice of the cathode position. For the vertical-drift (VD) design, the cathode is suspended horizontally mid-way between the top and bottom of the module [8]. For the horizontal-drift (HD) design, the cathode planes are positioned vertically [9]. An electric field is applied to the active LAr volume, with different drift directions (vertical *vs.* horizontal) and distances (6.5 *vs.* 3.6 m). Distinct charge readout technologies (copper strips printed on large circuit readout planes, CRPs, *vs.* wires wound in large anode planes assemblies, APAs) are used for the two modules. However, the Pandora Software Development Kit (SDK) [21, 22], which currently serves as the main package used in DUNE to provide pattern recognition algorithms to reconstruct the neutrino interaction, is agnostic to the detector differences, and specific orientations between incoming neutrino and detector drift directions were found to have mild effects. As a result, a comparable atmospheric neutrino reconstruction performance overall is expected for horizontal- and vertical-drift detector configurations, allowing this article to focus exclusively on the Horizontal-Drift detector.

Charged particles passing through LAr ionize and excite the argon atoms producing ionization electrons and scintillation photons. These photons are detected by DUNE's Photon Detection System (PDS) and reconstructed as a collection of flashes [2]. It was checked that every selected atmospheric neutrino interaction for which results are reported has an associated reconstructed PDS flash. In addition, charge-light mismatches, which incorrectly combine atmospheric neutrino TPC information with reconstructed PDS flashes produced by unrelated, and lower-energy, radiogenic-induced energy deposits, are also expected to be small in this energy range. Therefore, t_0 and drift distance determination is assumed to be perfect

in the following, and no further use of the PDS information is made in this paper.

The ionization electrons are carried by the electric field to the APA, where three layers (u , v , and w) of active wires (vertically oriented for the w plane, and at $\pm 35.7^\circ$ to the vertical for u and v planes), form a regular grid for collection and induction of ionization charge readout. The relative voltage between the planes is chosen to ensure all but the final layer (w) are transparent to the drifting electrons. The right-handed Cartesian coordinate system used to describe the detector geometry, depicted in Fig. 1, has x as the drift axis, y as the upwards vertical direction, and z the remaining orthogonal direction. While in the case of beam neutrinos z is the primary direction, for atmospheric neutrinos the zenith angle θ_y^{true} is used throughout the paper when reporting reconstruction performance dependence on neutrino direction. This choice is motivated by θ_y^{true} being the only relevant angle for sensitivity studies with atmospheric neutrinos. For each readout plane, localized charge deposits (*i.e.*, hits) are identified from the collected or induced charge waveforms, with each plane (u , v , w) providing a 2D ‘view’ (U, V, W, respectively) of particle interactions in the LArTPC.

The three sparse lists of 2D hits (hit wire and time) are provided as input to Pandora’s large number of decoupled algorithms to develop the reconstruction from hits to particles, with each algorithm designed to address a specific aspect of pattern recognition. DUNE’s software [23] builds directly on the Pandora developments completed for another LArTPC detector, MicroBooNE [21]. The most important output of the pattern recognition is the list of Particle Flow Particles (PFPs). Each PFP is associated with: i) a list of 2D clusters, which group together the relevant hits from each readout plane based on their topological associations; ii) a set of reconstructed 3D positions, which combine the 2D information from the three planes for each cluster; and iii) a reconstructed vertex position, defining the PFP’s interaction point. As part of the PFP reconstruction, Pandora also provides a score describing how likely the PFP is to be a track-like or a shower-like particle, *i.e.*, whether its energy depositions in the detector are more like that of a muon, a pion, or

of a proton (linear pattern) or like that of an electron or a photon (spray pattern). The PFPs are placed in a hierarchy, corresponding to their identified parent-child order, *i.e.*, which ‘child’ particle was produced during the decay or interaction of a ‘parent’ particle. A neutrino PFP will be the primordial parent for a neutrino interaction. An identification of each particle, as well as the flavor determination for the neutrino, can also be made, and some results will be discussed in this paper.

Hereafter, a simulated event is defined as a single readout window of 2.25 ms—spanning the full ionization electron drift time—aligned such that the neutrino interaction occurs at $t_0 = 0$. Given the rock overburden, the rate of cosmic ray muons is expected to be approximately $\mathcal{O}(10^{-4})$ per readout window in the full volume of a horizontal drift module, and therefore no cosmics are simulated. Neutrino interactions are generated using GENIE v3.04.00 [24, 25] with the Liquid Argon Experiment tune AR23_20i_00_000, the propagation of particles and their interaction within the detector are simulated by Geant4 v10.6.p01f [26–28] with the QGSP_BERT physics list, and the detector response is simulated using LArSoft v09_81_00 [29, 30]. The physics parameters used for the LArTPC simulation have been informed by the ProtoDUNE reported performance and measurements [31, 32]. In order to lower the time and computing resources required to process the large sample used for the studies presented in this paper, a reduced version of the HD module was used for the detector simulations, the so called ‘1x2x6’ geometry, shown in Fig. 1, consisting of one plane of APAs (2-APAs tall and 6-APAs long) and two cathode planes assembly (CPAs), situated one drift-length away on either side of the APAs plane in x . This active-volume representation, $719\text{ cm} \times 1208\text{ cm} \times 1394\text{ cm}$ ($x \times y \times z$), has the same height, about half the width, and a quarter of the length of the full HD module [33]. Wire-Cell v0_24_3 is used to simulate the electronics and field response, and to process the signal, along with the basic processing of the readout waveforms, which involves the deconvolution of the electric field response and noise removal in order to recover the ionization signals [34]. Hit finding is performed by LArSoft by fitting Gaussian functions to peaks in the waveforms. The

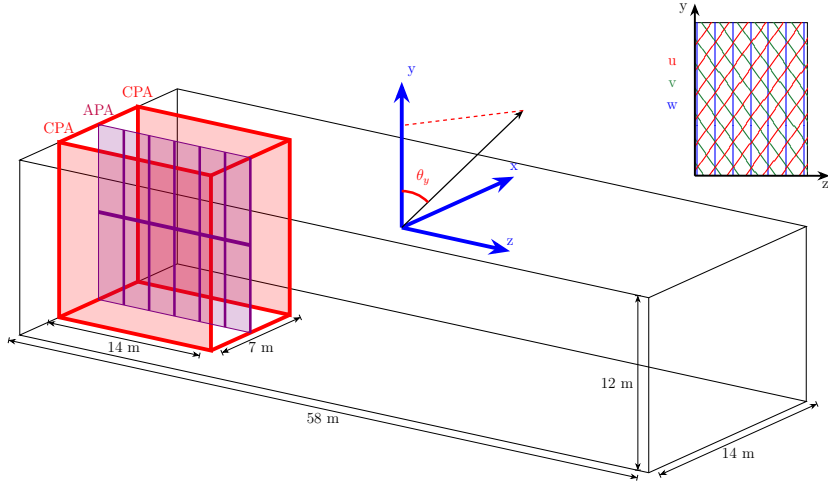


Fig. 1: At-scale depiction of the ‘DUNE HD 1x2x6’ geometry (red) within the full HD module geometry (black). The plane of APAs (purple) is flanked by the two CRP planes (light red). Also shown, the wires layout of the planes u , v , and w , together with the right-handed coordinate system used in which the zenith angle (θ_y) is marked.

resulting hits are fed into Pandora pattern recognition algorithms, with the high-level reconstruction being made using LArPandora v9_21_12, which depends upon PandoraSDK v03-04-01 [22].

With these settings, a sample of ~ 12 million atmospheric neutrinos with energies between 0.1 GeV and 10 GeV was generated. The interactions are isotropically generated in the entire active volume of the reduced geometry used, with no interactions generated outside this volume. The sample contains charged current (CC) and neutral current (NC) interactions for all the neutrino flavors according to their relative cross-section ratios as computed by GENIE. An exponential energy flux spectrum ($E^{-2.5}$) with isotropic directions is used for this generation in order to have a sufficient number of interactions at higher energies. No further manipulation was done to the spectrum (*e.g.*, reweighting with the atmospheric neutrino flux expected at the Homestake mine [35], or considering oscillation probabilities, *etc.*), as the reconstruction performance results were studied separately for ν_e and ν_μ ; any further physics discussion is outside the scope of this paper. As such, the interaction rate differences, which can be seen in Fig. 2, are solely shaped by the cross-section differences between different flavours, as implemented in GENIE.

MC statistical uncertainties, displayed as vertical error bars, are reported for all following figures.

2.2 Vertex fiducialization and interaction containment

A fiducialization selection was applied on the full sample, requiring the reconstructed primary vertex position to be further than 20 cm from all the LArTPC walls. This selection: i) helps to maximize the statistical reach of the sample, while cleaning events with interactions at the edge of the active volume, which are poorly reconstructed; and ii) mimics a similar selection that will have to be used by any future physics analysis to remove neutrino interactions that are harder to distinguish from external backgrounds. Since the vertex position is reconstructed from all the hits of the event, and it is the starting point for the rest of the high-level reconstruction in the event (tracks, showers, particle identification, *etc.*) it was seen as a reliable reference to use in deciding on a fiducial volume (FV) selection. An additional requirement is that Pandora reconstruct at least one final state particle (track or shower), which allows for the inclusion of events that actually have detected final state particles to conduct any analysis with.

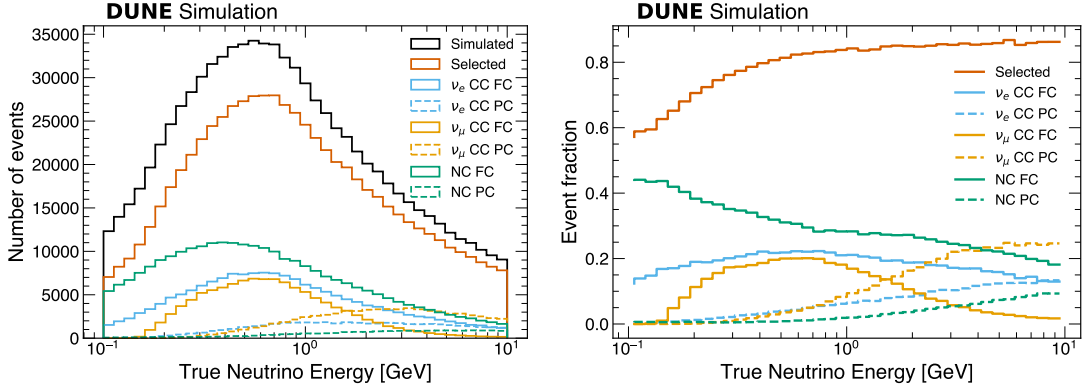


Fig. 2: Neutrino energy distributions for CC and NC events separated in various categories. ‘Simulated’ label corresponds to all simulated events, while ‘Selected’ label refers only to events passing the fiducial volume (FV) cut as well as the reconstructed final state particle selection. The number of events (Left) and the event fraction (Right) with respect to the amount of simulated events per bin, for fully contained (FC) and partially contained (PC) events.

Atmospheric neutrino interactions can occur in the full LArTPC volume, with any incoming direction. Most of these neutrinos have a relatively low energy ($< 1 \text{ GeV}$), and consequently the full chain of interactions they produce will have a relatively small spatial extent in the detector. However, the atmospheric flux also features high energy neutrino interactions with a very large extent in the detector, for which part of the final state particles can be uncontained. So the last aspect of the selection considered in this paper is related to the containment of a neutrino interaction (*i.e.*, whether its energy is fully or just partially deposited within the LArTPC volume). The FD-HD is expected to record both fully contained (FC) and partially contained (PC) atmospheric events in DUNE, and all of them can be considered for physics analyses. However, different reconstruction performance is expected for FC and PC events, in particular for the energy resolution. In order to best capture the effects of containment on atmospheric neutrino physics in DUNE, the analysis sample was split into FC and PC sub-samples, based on the following chosen criteria: the FC (PC) sub-sample contains neutrino events for which no (at least one) hit belonging to a reconstructed final state particle by Pandora is present outside the fiducial volume. It should be noted that no radiological background (arising from the natural contamination of radioactive isotopes in detector materials and the

surrounding cavern) was considered in this study, as they are primarily visible in neutrino LArTPCs via MeV-scale signatures [36], which are outside the energy range studied in this paper.

Figure 2 shows the effect of all these selections as a function of the true neutrino energy. The FV and the ‘at least one reconstructed final state particle’ selections filter mostly low-energy neutrinos. The splitting into the FC and PC categories has, as expected, a very strong energy dependence, since most of FC events correspond to low-energy neutrinos (below 1 GeV). In addition, there is also a neutrino type dependence, because ν_μ events are less easily contained than ν_e , as the rate of energy loss of the muon in the liquid argon is much smaller than that of the electron (*e.g.*, a 1 GeV muon travels for ~ 34 radiation lengths in LAr).

3 Atmospheric neutrino event reconstruction

3.1 Neutrino-interaction vertex finding

The neutrino interaction vertex is the point from which all charge depositions in the detector emanate, and many Pandora algorithms (as well as other high-level reconstruction observables like PID, direction, *etc.*) leverage it as an anchor point to reconstruct the emitted final-state particles. The original [22] Pandora vertex-location

finding algorithm was re-written in DUNE to use a convolutional neural network (CNN) [33]. The architecture of the network is kept exactly the same for beam and atmospheric neutrino events, with two stages of processing: pass one is a coarse search to define the correct region within an event for the vertex position, pass two is a more detailed search within that region. The only difference between beam and atmospheric vertex finding is that the network is trained separately on the two samples, for two reasons. First, a CNN trained only on beam events leads it to give a specific importance to the beam direction with respect to any other direction, leveraging this information of the beam direction to easily break ambiguities in the vertex location for these type of events. However, as atmospheric neutrinos can come from any direction, using a CNN trained on beam events would introduce a bias. Second, the atmospheric neutrinos have a different flux than beam neutrinos, with a greater fraction of neutrinos expected below 1 GeV.

The CNN training for the atmospheric events was performed directly on a subset of 600 K events (from the whole sample), reconstructed up to the stage of the 2D hit reconstruction, without any further selection. The training was performed in a staged way (as for the beam [33]), one for each of the two passes of the vertex reconstruction algorithm: the first pass was retrained first before being used to retrain the second pass. The obtained vertex resolution is shown in Fig. 3, for CC only (as they are guaranteed to have vertex activity), FC and PC events, in each direction. The performance is comparable to that obtained for beam events [33], with resolutions below 1 cm for each plane. The degraded performance in the y axis case can be explained by the orientation of the collection plane's wires in particular: they are collinear with y , and thus provide less spatial resolution in this direction. It can be seen that the containment of the interactions has a minimal impact on this performance, and the same was found for the flavor of the neutrino.

Figure 4 shows the proportion of events for which the vertex is reconstructed within 1 cm of the true vertex location in a given direction as a function of the true neutrino zenith direction, in three neutrino-energy intervals: 0.1 – 1, 1 – 5, 5 – 10 GeV. This efficiency allows the

characterization of the quality of the vertex reconstruction for a given subset of events. The 1 cm threshold is chosen as this is in the large majority of cases an accuracy sufficient to ensure the quality of downstream Pandora reconstruction. An increased vertex reconstruction efficiency is observed for neutrinos propagating orthogonally to the y direction, with average efficiencies of 82% and 80% *vs.* 76% (87% and 85% *vs.* 80%) for the lowest (highest) energy bin shown in x , z and y directions, respectively. The dependency on neutrino propagation direction increases with the neutrino energy, as expected by the fact that the produced final state particles will be more and more boosted in the true neutrino direction as the energy increases, and thus show more clearly the effects of the neutrino directionality on the reconstruction performance.

3.2 Particle reconstruction

3.2.1 Efficiency, purity, and completeness

The metrics used for assessing the particle reconstruction performance in this subsection are the following:

- **Purity:** the fraction of hits in the reconstructed particle that are matched with that of the corresponding generated particle, $N_{\text{recoHits}}^{\text{matched}} / N_{\text{recoHits}}$;
- **Completeness:** the fraction of hits in the generated particle that are matched with the corresponding reconstructed particle, $N_{\text{genHits}}^{\text{matched}} / N_{\text{genHits}}$;
- **Efficiency:** the fraction of a type of target MC generated particles matched to a reconstructed particle. In order to ensure that the reconstructed PFP is associated with a single MC particle, the matching criteria used are: i) at least 5 shared hits, in order to avoid the metric being skewed by small clusters from things like neutron capture; ii) and purity and completeness levels of at least 50%, to ensure that the majority of the hits in the PFP are associated with the MC particle, while excluding matches between target MC particles and small, fragmented reconstructed particles. Double counting is also avoided in the way the counting is set.

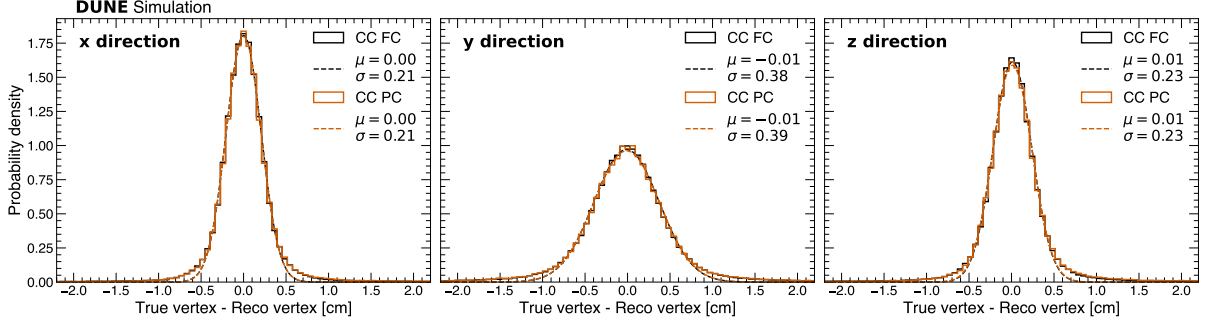


Fig. 3: Resolution distributions of the reconstructed primary interaction vertex, for (from Left to Right) the x , y , and z directions, for CC interactions, with all flavors combined. The mean (μ) and standard deviation (σ) for each distribution are also listed.

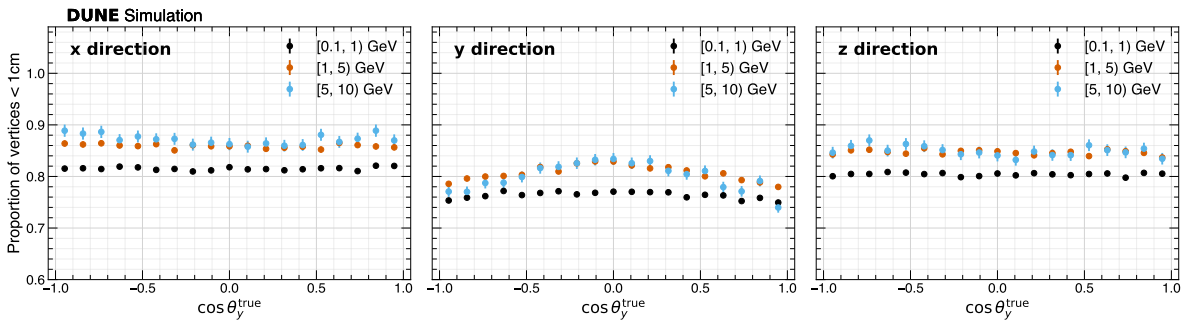


Fig. 4: Proportion of vertices reconstructed within 1 cm in a given direction from the true vertex, as a function of the zenith angle θ_y^{true} , for (from Left to Right) the x , y , and z directions. Results are shown for three neutrino-energy intervals, for CC FC events only.

A subsample of ~ 1.5 M events from the large 12 M sample has been used for the studies in this section. The events are required to pass the vertex fiducialization selection, without any further requirement on containment.

The results are shown in Fig. 5, combined for CC and NC neutrino interactions. The reconstruction efficiency of muons is the highest among all particles over the full energy range shown, and rather flat. For protons, the efficiency shows a sharp decrease above ~ 1 GeV, caused by the fact that protons below this energy mostly leave tracks in the detector, while above they tend to produce hadronic showers, which are more difficult to reconstruct. Additionally, high-energy protons are associated with complex deep inelastic scattering (DIS) topologies in which most of the hits are clustered together into a large shower by Pandora.

At low energies, below ~ 300 MeV, the efficiency drops for all particles: for muons and electrons, this is due to high-energy neutrino interactions where the charged lepton carries a smaller fraction of the energy and may be clustered with more energetic hadronic or photonic showers. For protons and photons, the same issue occurs, compounded by the intrinsic difficulty in detecting particles that leave very few hits and are easily absorbed into nearby lepton PFPs. At high energies, above ~ 2 GeV, photon reconstruction efficiency improves, as they tend to carry a significant fraction of the neutrino energy and are more easily matched to reconstructed objects due to the matching algorithm prioritizing shared hits. Pions exhibit behavior similar to protons, though slightly worse at low energy, as their reconstruction is more strongly impacted by the complexity

of the interaction topology they are usually associated with. Muons remain the best-reconstructed species across all metrics due to their long, clean track-like signatures. All these considerations are reflected also in the completeness and purity results, with highest performance for muons and poorest for photons.

3.2.2 Particle identification method

The 3D high-resolution tracking and the 4π calorimetry capabilities of the LArTPCs are what distinguishes them from other neutrino detection technologies. The particle identification that these characteristics will enable in DUNE should allow for a superior neutrino direction and energy reconstruction performance. The measurement accuracy of these quantities improves when knowing precisely the type of the particle (muon, pion, electron, proton, ...) depositing energy in the LAr, as different particles have different energy deposition profiles, and therefore different amounts of charge recombination (*i.e.*, ionization electrons that recombine with argon ions). Identifying the particles and thereby correcting/calibrating their kinetic energy (E_{kin}) and extracting their momenta accordingly improves neutrino reconstruction, as shown in Secs. 3.4 and 3.3. Two phases can be distinguished in the particle identification (PID) process: the separation between track-like and shower-like objects, and then the identification among these of the different particle types.

The separation between track-like and shower-like objects is performed by a Boosted Decision Tree (BDT) integrated within Pandora [21] that was retrained on a subset of the atmospheric sample. Hyper-parameters such as the number of training examples and the learning rate were optimized based on a subsample of ~ 1.5 M events. The final training was made on a distinct sample containing $\sim 190\,000$ PFPs reconstructed with purity and completeness above 0.5. The obtained results can be seen in the left panel of Fig. 6, following the convention established by MicroBooNE [37] for the definition of the Track-like and Shower-like particles. Applying a cut on the BDT score at 0, allows to select tracks with an efficiency of 89 % while rejecting 91 % of the showers.

The approach taken for performing PID, to separate highly ionizing particles (e.g. protons)

from minimum ionizing particles (e.g. muons), was to deploy the PIDA [38] phenomenological model to characterize the Bragg peak. A PIDA score was calculated, which relies on the power-law dependence of $\frac{dE}{dx}$ on the particle residual range, as it reaches the end of its travel within a medium:

$$\frac{dE}{dx} \simeq AR^b \quad (1)$$

where R is the residual range, b is a constant varying weakly with the particle type (-0.42), and A is a proportionality coefficient, which varies with the particle type, and is to be measured. The PIDA score is calculated for each reconstructed Pandora track on its last 30 cm (or less if the track is shorter) as:

$$\text{PIDA} = \frac{1}{N_{\text{points}}} \sum_i^{N_{\text{points}}} \left(\frac{dE}{dx} \right)_{\text{reco},i} R_i^{0.42}. \quad (2)$$

The results displayed in the right panel of Fig. 6 show a good separation between the proton and the muon/pion distributions. A selection requirement of $\text{PIDA} > 10$ retains $\sim 87\%$ of the protons with a purity of 91%. However, it can also be seen that there is very little separation power between the charged pions and muon tracks, which can be understood from them having a very similar $\frac{dE}{dx}$ profile. The specific double peak feature for pions was understood by the two types of pions tracks reconstructed in the detector. One, corresponding to stopping pions, will have the expected energy deposition profile from an ionizing particle of this mass, and as a consequence, the associated PIDA score will be computed correctly. The other, from pions undergoing inelastic hadronic interactions, have the end of their track not corresponding to a particle at rest, and therefore, the residual range R used for the PIDA calculations will be wrong, and this will lead to a shift to lower PIDA values of the particle. Even though the possibility to explicitly tag pions undergoing an inelastic hadronic interaction with PIDA and apply a specific treatment to them in the reconstruction seems promising, it has not been applied here and it is left for future work. Similarly, an accurate discrimination between charged pions and muons should be possible by considering additional geometric features

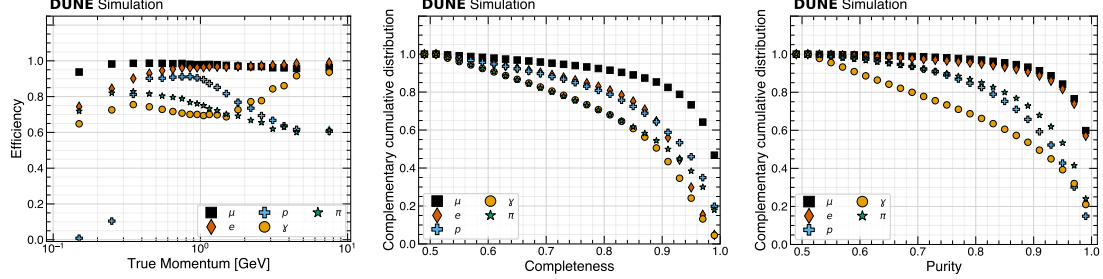


Fig. 5: Efficiency versus true particle momentum (Left), and complementary cumulative distributions for completeness (Middle) and purity (Right). The complementary cumulative distributions represent the fraction of events with completeness/purity above a certain x-value.

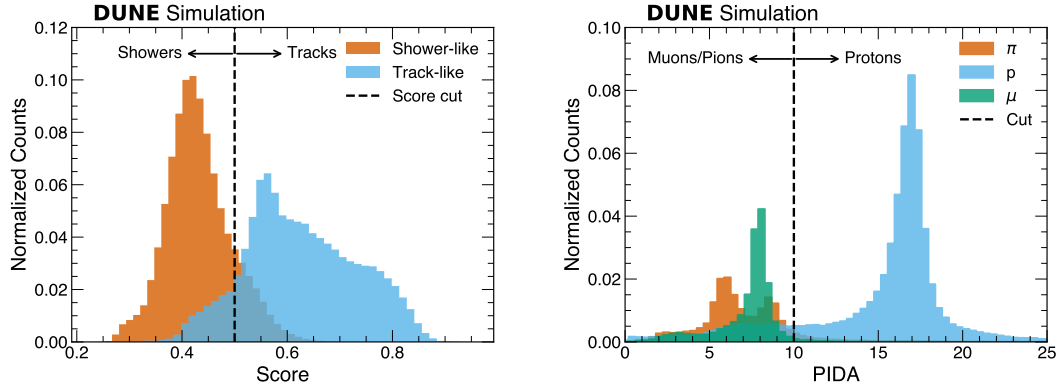


Fig. 6: Distributions of the classification scores: (Left) Track-Shower BDT scores; (Right) PIDA scores for Pandora tracks split into the true particles they are associated with.

such as the track scattering or the track lengths, but do not consider it in the following studies.

3.2.3 Direction reconstruction

An accurate determination of individual final-state particle direction is essential for the reconstruction of atmospheric neutrinos. This is because for these types of neutrinos, there is no knowledge of the traveling direction, hence no knowledge about the distance traveled, which directly impacts any oscillation measurement. This reconstruction of the direction is made by two separate algorithms, one for tracks, and one for the hadronic and electromagnetic showers. In the track reconstruction module, a Principal Component Analysis (PCA) is first applied to define a local 3D coordinate system aligned with the track's principal axis. Subsequently, a sliding-window linear fit is performed on the constituent

2D hits. This method reconstructs the track using a series of local segments, which are combined to yield 3D trajectory points and estimate the overall track direction. In contrast, the shower module reconstructs direction by applying PCA directly to the spatial distribution of the 3D hits. The actual pointing of the shower is made in the direction of the largest spatial extent.

The left panel of Fig. 7 shows the resolution on the reconstruction of particles direction with respect to the y direction (most relevant for any atmospheric neutrino oscillation analysis) for all types of particles. Both the fully and partially contained particles are considered as the containment was checked to only have a minimal impact in this case. While the best direction resolution is obtained for muons, which have a resolution below 5° at a kinetic energy of 1 GeV, the following general trends can be observed:

- For all particles, the resolution is relatively poor at low- E_{kin} (below 100 MeV), because the tracks or showers are shorter and the accurate reconstruction of their direction is more difficult. This is especially the case for proton tracks, which only span very few centimeters at these energies.
- For shower-like particles, the best resolution is obtained for E_{kin} between 100 MeV and 1 GeV, where the individual track/shower reconstruction is easy as they are all long enough, and the events are not very crowded.
- A degradation of resolution is observed at higher E_{kin} for shower-like particles, as the events become more and more crowded, and the accuracy in the reconstruction of the individual particles decreases. This is mainly due to the over-clustering of the particle hits together in the last parts of the reconstruction process.

In general, electrons and photons show lower performance compared to other particles, especially at higher energies, because their showers are more likely to be confused with the overall hadronic system while tracks can more easily be separated from hadronic showers.

The right panel of Fig. 7, in which a selection cut $E_{\text{kin}}^{\text{reco}} > 10 \text{ MeV}$ was applied to all particles, shows that there is also a dependency of the angular resolution on the true initial direction of the particle itself. Muons direction resolution has little dependence on the true muon direction. On the contrary, other particles show a slightly stronger dependency, with the best resolutions obtained for particles orthogonal to the y axis. A loss of resolution is observed for tracks very aligned with y (or $-y$) direction, because of the lack of hits on the W view, whose wires are themselves oriented along the y direction, thus not providing any information for these tracks.

3.2.4 Energy reconstruction: muons

Reconstructing the muon energy precisely is of critical importance in order to accurately reconstruct the energy of muon neutrinos. Two methods are used for the energy reconstruction of muons in DUNE. If the reconstructed track is fully contained, the kinetic energy E_{kin} is calculated by range using the Constant Slow Down Approximation (CSDA) [39]. However, when the muon track is uncontained, it is not possible to rely on such

a method as it can only be applied to stopping muons. Escaping muons are not rare in the case of atmospheric neutrino interactions given the energy flux, the geometry of the detector and the direction of the neutrinos. This is why, in the context of the atmospheric reconstruction, additional muon energy reconstruction methods relying on the Multiple Coulomb Scattering (MCS) were intensively studied. One method, Chi2, is based on the OPERA and ICARUS [40, 41] experiments implementation, while another one, LLHD, is based on that of the MicroBooNE [42] experiment. While both methods are implemented in the DUNE reconstruction software at present, in the context of this paper, the focus is on the results obtained with the LLHD method, which was found to perform consistently better (*i.e.*, smaller biases and improved resolutions) than the Chi2 one in the case of atmospheric neutrinos.

In general in MCS approaches, the track is first divided into segments of length x , followed by a straight-line fit to the space points in each segment. The scattering angle between each pair of connected segments is calculated, and the obtained distribution of scattering angles for all segments belonging to a track is fitted with a Gaussian centered at zero, from which the standard deviation is computed. The procedure is repeated for six different segment lengths between 10 cm and 60 cm [40]. In the end, the scattered angle of the muon track, θ_0 , is the standard deviation of the Gaussian distribution and given by the Highland formula:

$$\theta_0 = \frac{13.6 \text{ MeV}}{\beta c p} z \sqrt{\frac{x}{X_0}} \left[1 + 0.038 \ln \left(\frac{xz^2}{X_0 \beta^2} \right) \right], \quad (3)$$

where βc , p , z are the particle's velocity, momentum, and charge number, respectively, and X_0 is the radiation length of LAr (assumed constant and equal to 14 cm). For the LLHD method in particular, only the scattered angles $\Delta\theta$ of 10 cm segments are considered. Given the normal probability of the scattering angle

$$f(\Delta\theta) = \frac{1}{\sqrt{2\pi\theta_0^2}} \exp \left[-\frac{1}{2} \left(\frac{\Delta\theta}{\theta_0} \right)^2 \right], \quad (4)$$

the likelihood is estimated by the product of $f(\Delta\theta_i)$ over all $n = n_{\text{segments}} - 1$ scattering angles

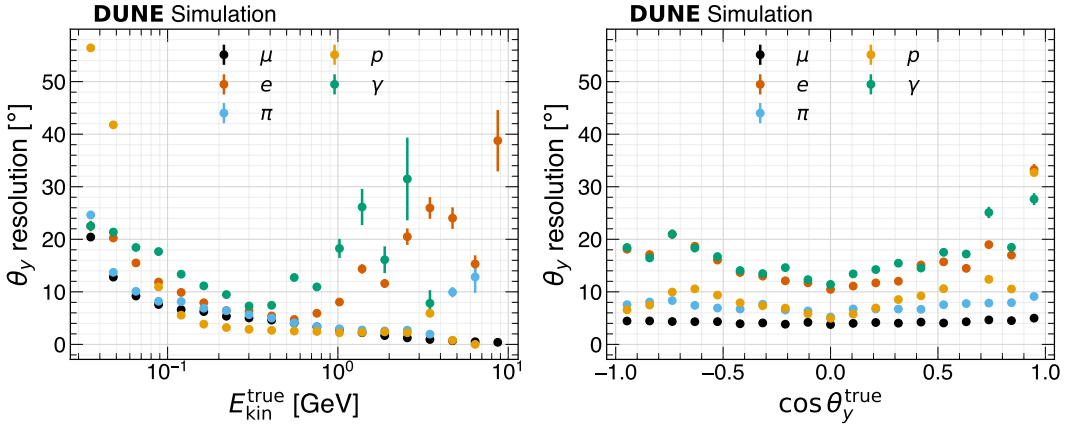


Fig. 7: Resolution of reconstructed particle's angle with the y direction (θ_y), as a function of (Left) particle's true kinetic energy $E_{\text{kin}}^{\text{true}}$, and (Right) of $\cos(\theta_y^{\text{true}})$, for muons, pions, electrons, protons, and photons.

$\Delta\theta_i$ [42], and the momentum is measured by minimizing the negative log likelihood:

$$-\ln(L) = \frac{n}{2} \ln(2\pi) + \sum_{i=1}^n \ln(\theta_{0,i}) + \frac{1}{2} \sum_{i=1}^n \left(\frac{\Delta\theta_i}{\theta_{0,i}} \right)^2. \quad (5)$$

In order to compute the expected scattering angle using Eq. 3, Eq. 5 takes into account the momentum of the particle in each segment. Therefore, the energy loss throughout the segments needs to be taken into account. In the minimization process, this energy loss is computed using the most probable energy loss dE/dx value (MPV) in liquid argon [39]. In addition, Ref. [42] has tuned Eq. 3 for LAr, and found that the value of 13.6 MeV depends on the particle's momentum. This tuning, however, depends on how the scattering angle is being computed and how the energy loss is being taken into account. Because of this, and following a similar approach as Ref. [42], Eq. 3 was modified to the form

$$\theta_0 = \frac{\kappa(p)}{\beta cp} z \sqrt{\frac{x}{X_0}} \left[1 + 0.038 \ln \left(\frac{xz^2}{X_0 \beta^2} \right) \right], \quad (6)$$

in which the $\kappa(p)$ parameter is fitted as function of the true momentum, in each segment.

Figure 8 shows the resolution and bias distribution of reconstructed energy when using the CSDA and LLHD methods in its left panel. The CSDA method shows extremely good performance

($\sim 2\%$ resolution) across the energy range. A cut is applied at 3 GeV because too few muons are contained in the simulated geometry above this energy. With the MCS LLHD, the resolution is of course degraded, but this method allows to obtain a 25% energy resolution on the majority of uncontained muons below 1 GeV, which allows to obtain a reliable energy measurement even for partially contained ν_μ CC events. At higher energies, this method becomes limited by the intrinsic resolution of the detector that becomes unable to measure the small scattering angles of the muon, hence leading to an underestimation of the muon momentum and a large negative bias.

The simulation used for this paper uses only about 1/8th of the full detector geometry volume (with full vertical length). In the full-size detector, muon tracks will be longer, and two things are expected to change: (1) more tracks will be tagged as contained and (2) for exiting tracks, for a fixed energy, the fraction of the track-length inside the TPC will increase. Therefore, a better bias and resolution are expected when using CSDA in case (1) or MCS in case (2). This can already be seen in the right panel of Fig. 8, which shows the resolution and bias of the MCS calculation versus the relative length inside the TPC, defined by the ratio of the reconstructed length to the expected length computed using the CSDA method on the true muon momentum. One can notice the improvement in energy reconstruction

when the tracks have a higher relative length inside the TPC.

In Fig. 8, and all other figures of the same type in the rest of the paper, the relative resolution and bias are shown as a band plot where the main line corresponds to the relative bias while the $\pm 1\sigma$ asymmetric resolutions are shown as the distance between the bias line and the upper (lower) band extremity respectively. They have been computed in the following way:

- **Relative bias:** is calculated as the mean value of the $(\text{reco} - \text{true})/\text{true}$ ratio, for a given variable, for all events falling into a given bin.
- **Relative resolution:** is estimated following several steps: i) the events are sorted into bins of a given variable; ii) for all events within each bin, the $(\text{reco}/\overline{\text{reco}})$ distribution is evaluated, where $\overline{\text{reco}}$ is the mean value of the reco variable within the bin; iii) for each bin, the 16 % and 84 % quantiles of the distribution are evaluated; iv) this inter-quantile measurement is divided by 2, corresponding to the definition of one standard deviation in the case of a gaussian distribution.

3.2.5 Energy reconstruction: electrons

Electrons with an energy in the GeV range produce electromagnetic showers in the detector that develop as the electron emits bremsstrahlung gamma rays, which in turn create electron/positron pairs. The typical extent between the vertex and the maximum of energy deposition of the shower is given by

$$l \simeq X_0 \log(E/E_c), \quad (7)$$

where $X_0 = 14 \text{ cm}$ is the radiation length and $E_c = 32 \text{ MeV}$ is the critical energy for electrons. It is calculated that for an electron energy $E = 3 \text{ GeV}$, this length will be around 68 cm. However, photons can be radiated quite far from the main shower, and there are a lot of event-to-event variations in the actual shower profile. It has in fact been shown that for 1 GeV (3 GeV) electrons, on average 97 % of energy is deposited within a distance of 1.5 m (1.7 m) from the primary vertex [43]. This indicates that most of the electromagnetic showers produced by electrons will be contained in the detector. As such, it is

possible to reconstruct the energy of these electrons by using a calorimetric measurement of the total energy deposited in the shower.

The energy reconstruction of showers is performed the following way. For each of the three LArTPC views, a calorimetric sum of all the hits constituting a given PFP is calculated. This calorimetric sum corrects for the charge attenuation during the drift and an average recombination factor. A charge to energy conversion is also applied according to some fixed gain calibration factors. Among the three readout planes of the DUNE HD detector, the w collection plane is the one with the highest signal-over-noise ratio and as a consequence the most accurate in estimating the energy. It even provides a more accurate energy estimate than the particle-by-particle "best view" (*i.e.*, the view that collected the highest number of hits from a given particle). As a consequence, it is the W view that was used to perform the calorimetric estimation of the energy for the results shown here. The obtained resolution for electron showers is shown in the left panel of Fig. 9 for both FC and PC events. The PC events yield very similar results to the FC one, at the exception of some broadening in the energy resolution at higher energies. At low electron energies, the energy resolution is limited by the detection thresholds of the particles in the shower as several soft electrons produced in the shower do not deposit enough energy to be correctly detected as hits. In the current reconstruction, the hit detection threshold corresponds to roughly 300 keV, but even with hit-finding thresholds as low as 100 keV part of the deposited energy in shower could still not be detected [43]. The best performance is obtained for 1 GeV electrons, with an energy resolution around 15 %. An energy bias is present at energies $< 200 \text{ MeV}$ due to the detection inefficiencies before reaching 0 for all the higher energies.

3.2.6 Energy reconstruction: charged hadrons

Both protons and charged pions deposit energy continuously in the detector through ionization, leaving tracks in the detector just like muons. But there are some differences to take into account with respect to the muon case.

First, protons are often non-relativistic in DUNE due to their large mass. As a consequence,

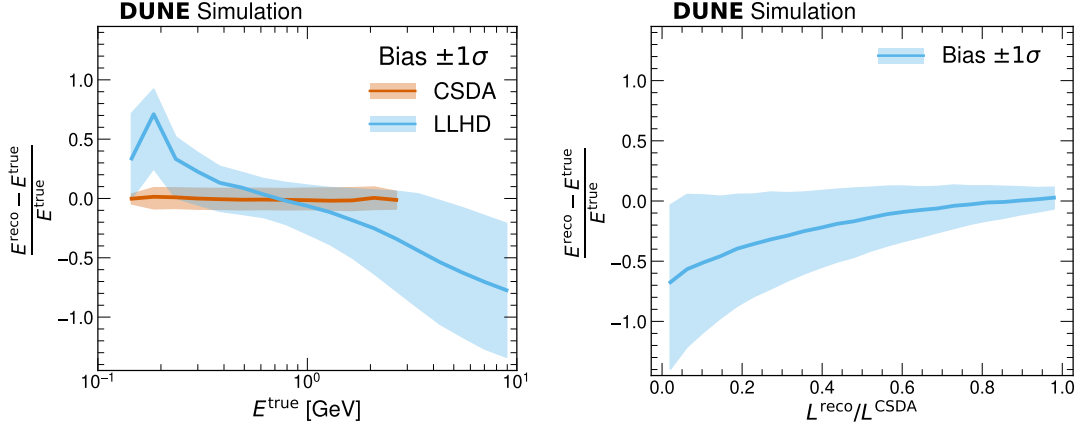


Fig. 8: Energy resolution and bias: (Left) versus true muon energy for the CSDA and LLHD methods, when requiring the longest track to be fully or partially contained, respectively; (Right) versus relative length inside the TPC for the LLHD method and partially contained longest tracks only. The L^{CSDA} refers to the expected muon track length computed using the CSDA method on the true muon momentum.

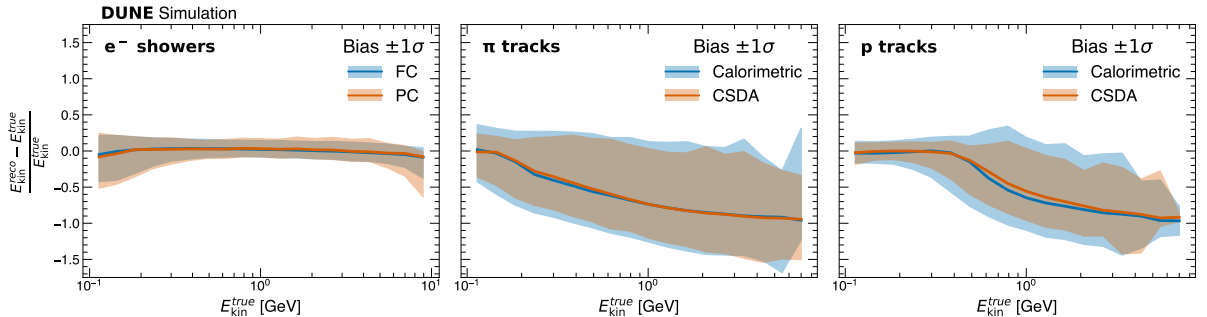


Fig. 9: Energy resolution and bias as a function of the true energy for: (Left) electron showers in fully (FC) and partially (PC) contained neutrino events; and for pion (Middle) and proton (Right) tracks in FC events only, when using two energy reconstruction methods.

their rate of energy deposition is larger by a factor of six with respect to muons, which leads to much shorter tracks. Moreover, this higher rate of energy deposition implies a higher charge-recombination rate. Second, charged hadrons can undergo hadronic (inelastic) scatterings in LAr, which become relevant for pions and protons with energy larger than a few hundred MeV. The typical exchange of energy in this kind of process is relatively large, with a cross-section that is relatively particle and energy independent and with an associated interaction length in DUNE around 1 m [43]. The scatterings cause loss of visible energy via nuclear breakup or recoil, or

by transfer of energy to neutral or very massive charged particles, which are left undetected in the detector. Consequently, if using a calorimetric energy measurement (in which the energy is calculated as the sum of the reconstructed charge of each hit of the particle's track, corrected for recombination and drift attenuation effects), the obtained energy resolution for these charged hadrons is bimodal: there is one peak around $E_{\text{reco}} / E_{\text{true}} \sim 1$ corresponding to particles not undergoing hadronic interaction, and a second wider distribution below $E_{\text{reco}} / E_{\text{true}} \sim 0.5$, corresponding to particles undergoing hadronic interaction which leads to a loss in visible energy.

The CSDA method suffers from the same limitations as the calorimetric energy reconstruction because of the hadronic interactions. Above 250 MeV of kinetic energy, there is a significant pion fraction that undergoes hadronic interactions, and for which the energy is underestimated. This can be clearly seen in the middle panel of Fig. 9 as an increase in the relative energy bias. When comparing the calorimetric and CSDA methods, the energy resolution is slightly better when using the range-based method, however the obtained resolution ranges from 30% to 60% below 1 GeV of kinetic energy. New methods trying to fit the energy of tracks undergoing hadronic interactions in LArTPCs are currently being developed [44], and it is foreseen to implement them in the future. For this paper, when needed for the neutrino direction reconstruction, the CSDA method is used for the energy reconstruction of protons, and the calorimetric one for that of pions (as the method less-sensitive to mis-PID).

The situation is very similar for protons, as it can be seen in the right panel of Fig. 9. The two major differences from pion are: i) the energy regime in which hadronic interactions impair the energy resolution is higher (>500 MeV); ii) the gain in resolution obtained by using the CSDA method is more significant. At low E_{kin} , where most of the protons lie, the energy resolution is around 15% for the CSDA method and 20% for the calorimetric method.

3.3 Neutrino energy reconstruction

In DUNE FD, both the energy of the lepton E_e^{reco} or E_μ^{reco} (already presented in Secs. 3.2.5 and 3.2.4, respectively) and of the hadronic system $E_{\text{had}}^{\text{reco}}$ can be reconstructed from the detected final state of a neutrino interaction. For the hadronic system, the reconstructed energy, $E_{\text{had}}^{\text{reco}}$ is calculated by adding all the registered hit energy depositions within the detector not associated with the tagged lepton. This reconstruction assumes an average recombination factor for all the particles, and doesn't use any PID information except for muons, the only particle for which a different method is used for the energy reconstruction, as presented in Sec. 3.2.4. In order to account for invisible energy within the detector

that differs for the leptonic and hadronic components as well as for the neutrino nature, the reconstructed (anti-)neutrino energy is defined as: $E_\nu^{\text{reco}} = \alpha E_{\text{lep}}^{\text{reco}} + \beta E_{\text{had}}^{\text{reco}}$, where α and β are scaling coefficients obtained for each flavor sample by minimizing the average bias on the reconstructed energy and can be found in Table 1. While a more complex method applying different scalings based on the event topology or dependent on the energy would possibly yield slightly better apparent performance, it would ultimately be more subject to systematic uncertainties in a physics analysis. This more simple combination of $E_{\text{had}}^{\text{reco}}$ and $E_{\text{lep}}^{\text{reco}}$ was adopted here to get a quick estimation of the neutrino energy resolution. Note that however an actual physics analysis fit would probably prefer to rely on the individual $E_{\text{had}}^{\text{reco}}$ and $E_{\text{lep}}^{\text{reco}}$ observables without the need to combine them. Neutrinos and anti-neutrinos of a given flavor are grouped together as they cannot be easily separated in the reconstruction. In this section, the NC interactions are disregarded, as the neutrino only transfers a fraction of its energy, and focus on CC interactions only.

Sample	α ($E_{\text{lep}}^{\text{reco}}$ component)	β ($E_{\text{had}}^{\text{reco}}$ component)
$\nu_e/\bar{\nu}_e$	1.32	1.41
$\nu_\mu/\bar{\nu}_\mu$	1.08	1.47

Table 1: Fitted scaling coefficients applied to reconstruct the total neutrino energy with minimal bias

3.3.1 Electron (anti-)neutrinos

In the case of electron (anti-)neutrino interactions, the reconstruction of the energy is fully calorimetric. The scaled $\beta E_{\text{had}}^{\text{reco}}$ calculated as mentioned above, is directly compared to the true energy of the hadronic system, $E_{\text{had}}^{\text{true}} = E_\nu^{\text{true}} - E_e^{\text{true}}$, in the left panel of Fig. 10. Two regimes can be noticed: one at relatively small hadronic energies, a region dominated by quasi-elastic interactions, where the resolution is the best ($\sim 40\%$ below 1 GeV); and a second one, at higher hadronic energies, where resonant and inelastic neutrino interactions, as well as inelastic hadronic interactions of the final state particles happen, leading to a loss in energy resolution ($> 70\%$ above 3 GeV). The resolution

is also better for ν_e than for $\bar{\nu}_e$ because the latter leads to the production of a primary neutron (which cannot be detected) instead of a proton.

The left panel of Fig. 11 shows the same performance metrics but for the reconstruction of the neutrino energy, E_ν^{reco} obtained by linearly combining $E_{\text{had}}^{\text{reco}}$ and $E_{\text{lep}}^{\text{reco}}$. The obtained resolution on E_ν^{reco} is below 15 % at low energy, and around 20 % at higher energies. Furthermore, the resolutions are very comparable for ν_e and $\bar{\nu}_e$, despite the worse performance obtained on the measurement of $E_{\text{had}}^{\text{reco}}$ for $\bar{\nu}_e$. This is directly due to the smaller transfer of energy to the hadronic system in the case of $\bar{\nu}$ interactions compared to ν interactions.

The energy reconstruction exhibits some dependency on the neutrino direction. The left panel of Fig. 12 shows that the main effect is a smaller reconstructed energy for neutrinos traveling in a direction orthogonal to the z direction, due to the arrangement of the plane wires and to the drift direction. This effect is however relatively small with a maximum absolute difference in the average energy bias between the orientations below 3 %.

3.3.2 Muon (anti-)neutrinos

In the case of muon (anti-)neutrinos interactions, the reconstruction of the energy is relying on the CSDA and MCS methods for the muon part, and on the calorimetric measurement for the rest of the system. The results obtained when directly comparing $\beta E_{\text{had}}^{\text{reco}}$ to $E_{\text{had}}^{\text{true}} = E_\nu^{\text{true}} - E_\mu^{\text{true}}$ are shown in the right panel of Fig. 10: they exhibit similar behaviors as in the electron (anti-) neutrino case at low-energy (35 % to 40 % resolution below 1 GeV). However, the obtained energy resolution on the hadronic system is significantly lower than in the electron neutrino case for multi-GeV neutrinos where it reaches $\sim 30\%$. This is expected by the fact that the discrimination between the lepton and hadronic system is easier if the lepton is a muon, which leaves a long track in the detector, than when it is a electron, which can produce wide showers overlapping with the hadronic system.

E_ν^{reco} is again obtained by linearly combining $E_{\text{had}}^{\text{reco}}$ and $E_{\text{lep}}^{\text{reco}}$ and the obtained results are shown in the two right-most panels of Fig. 11. The resolution on E_ν^{reco} is below 10 % at low energy,

and around 15 % at higher energies for FC events. Furthermore, the resolutions are very comparable for ν_μ and $\bar{\nu}_\mu$, despite the worse performance obtained on the measurement of $E_{\text{had}}^{\text{reco}}$ for $\bar{\nu}_\mu$ for the same reasons as above. Some difference can however be noticed on the bias of these two distributions at low and high energies due to an interplay between the differences in hadronic system and inelasticity distributions. As expected, events only partially contained don't allow to measure the energy in the most accurate way, especially for muons, hence leading to degraded neutrino energy resolutions for PC events. However the neutrino energy can still be measured with a resolution around 20 % for multi-GeV PC ν_μ events.

The right panel of Fig. 12 shows that the muon neutrino energy reconstruction is only moderately impacted by the incoming neutrino direction, with a slight loss of performance only noticed for neutrinos aligned with the drift direction x .

3.4 Neutrino direction reconstruction

3.4.1 Method

Three main algorithms have been developed to reconstruct the direction of the interacting neutrinos in the DUNE FD, which rely on different levels of information retrieved from the event reconstruction algorithms.

Using just the reconstructed primary lepton.

The simplest and most straightforward method for estimating the direction of the interacting neutrino uses only the information of the reconstructed primary lepton direction. The primary lepton particle is easy to reconstruct in DUNE FD, and as its direction tends to align with the neutrino's direction, as shown in Fig. 13, one can directly use the reconstructed lepton direction as reconstructed neutrino direction. This is especially true for antineutrino interactions, which have a lower inelasticity (*i.e.*, hadronic energy fraction) distribution than neutrino interactions. The obtained performance highly depends on the neutrino energy mostly because of Fermi motion: at lower energies the neutrino and target nucleon have similar momenta and the information on the

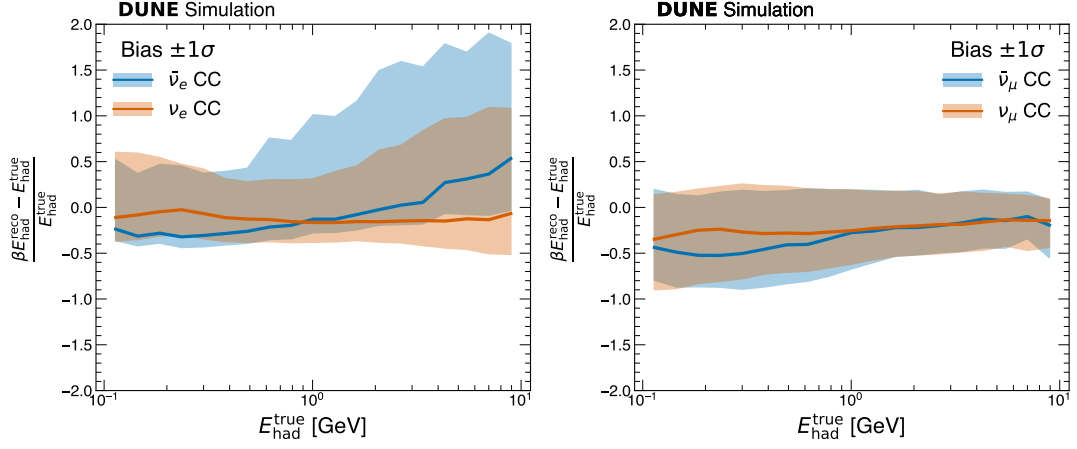


Fig. 10: Resolution and bias for the reconstructed hadronic energy $E_{\text{had}}^{\text{reco}}$ as a function of the true hadronic energy $E_{\text{had}}^{\text{true}}$ for: (Left) ν_e and $\bar{\nu}_e$ (Right) $\bar{\nu}_\mu$ and ν_μ .

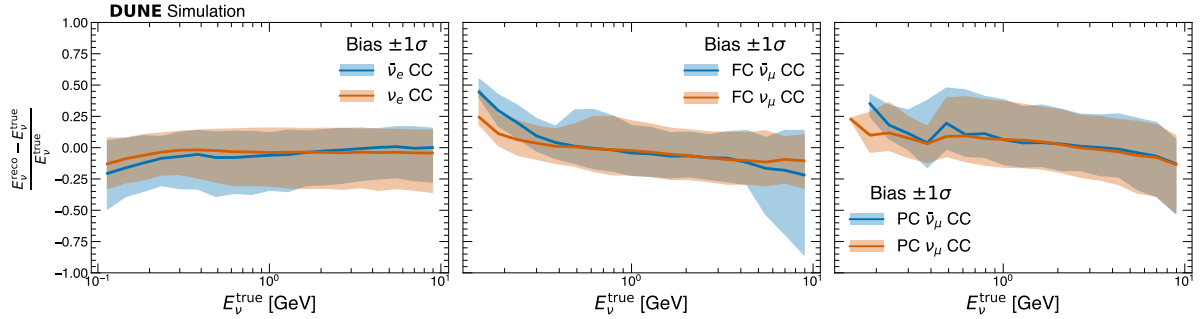


Fig. 11: Resolution and bias for the reconstructed neutrino energy E_{ν}^{reco} , as a function of the true neutrino energy E_{ν}^{true} for: (Left) ν_e and $\bar{\nu}_e$ FC (Middle) and PC (Right), $\bar{\nu}_\mu$ and ν_μ .

neutrino direction gets heavily smeared out in the final state. There are intrinsic limitations of this method: i) it performs poorly for NC interactions; ii) it does not take into account the other reconstructed particles of the event for a more complete calculation. This method is typically the one applied by Water Cherenkov detectors for atmospheric neutrinos with an energy below a few GeV because of the Cherenkov threshold, which often suppresses the visibility of the heavier hadronic system compared to the lepton. In practice in DUNE, it just means picking the most energetic reconstructed particle to be the lepton in the event.

Using all the reconstructed particles.

A second method to estimate the direction of the interacting neutrino is possible if the hadronic system can be reconstructed: it relies on the use of all reconstructed final state particles and summing their individual momenta, which implies the determination of their type/ID, energy, and direction. Reaching enough accuracy on these three metrics allows to improve the estimation of the neutrino direction with respect to the lepton-only method. The caveat of this method is that it can only be applied to events for which particles have been reconstructed.

A flowchart of this method is shown in Fig. 14. It starts with all PFP candidates, identifies their type, estimates their total momentum based on

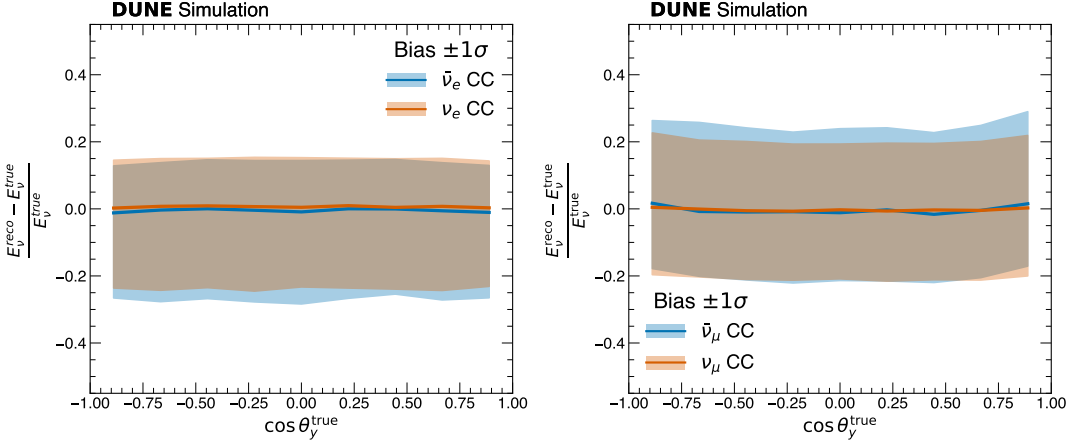


Fig. 12: Resolution and bias for the reconstructed neutrino energy E_ν^{reco} as a function of the neutrino direction along y , $\cos(\theta_y^{\text{true}})$ for: (Left) ν_e and $\bar{\nu}_e$; (Right) ν_μ and $\bar{\nu}_\mu$.

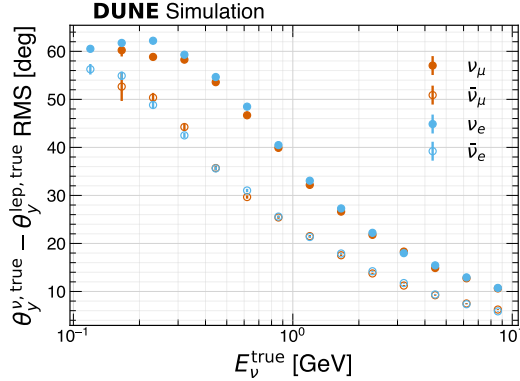


Fig. 13: The RMS of the difference between the true neutrino and the true primary lepton directions along y , as a function of the true neutrino energy, for CC interactions.

either the CSDA, MCS, or Calo (calorimetric estimation of the kinetic energy) method, which in the end is combined with their reconstructed direction to obtain the particles' 3-momentum. Once the 3-momentum of all the final state particles \vec{p}_i is obtained, the reconstructed neutrino direction \hat{p} is obtained as:

$$\hat{p} = \frac{\sum_i \vec{p}_i}{\|\sum_i \vec{p}_i\|} \quad (8)$$

As shown in the flowchart, the momentum of muons and protons is estimated by using the CSDA method as it allows to reach the best performance. However, the charged pions' momenta are estimated using the calorimetric measurement

of the energy depositions. This choice was made as this reconstruction method is less biased by pion inelastic scattering interactions.

Using only calorimetric hits.

A third method focuses on the determination of the neutrino direction using only the low-level reconstructed hit information in the 3 detector planes (u, v, w). The major advantage of this method is that it does not rely on any high-level particle-reconstruction information, and it can thus serve as a fallback method for any scenario in which the direction of an interacting neutrino is needed. It relies solely on the deposited energy, identifying the direction of the kinetic

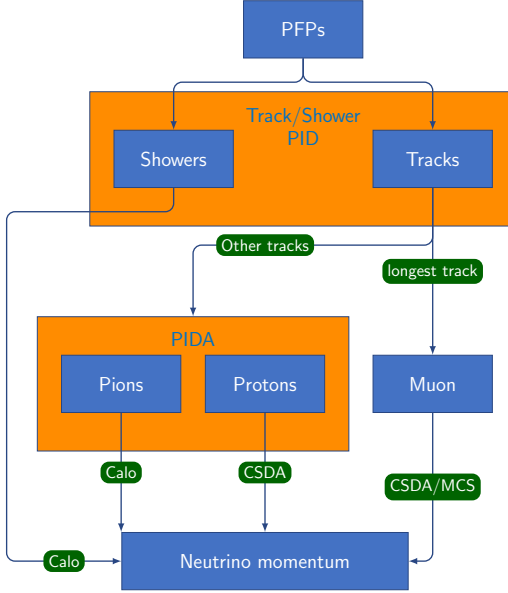


Fig. 14: Flowchart of the PID selection performed, and the methods used, to estimate the momentum of every of the final state particles when calculating the neutrino direction using all particles reconstructed in the event. The *Calo* refers to the method (calorimetric) deployed to estimate the kinetic energy of individual particles.

energy deposition to the momentum direction, without taking into account the various particle masses. The flow of this reconstruction method is the following:

1. For each of the 3 2D views (U, V and W), the reconstructed 2D hits are projected in the view coordinate system built from a normal vector to the wire direction and the time axis (associated to the drift direction). The hit coordinates in each view are shifted so that the reconstructed vertex lies at the origin.
2. The average 2D direction for each view (α^{view}) is calculated in the complex plane by averaging the direction to each hit from the origin (angle α_i with the time axis), weighted by the hit reconstructed charge (q_i): $\alpha^{\text{view}} = \arg(\sum_i q_i e^{j\alpha_i})$ where j is the imaginary unit. This hit reconstructed charge is corrected by the drift attenuation as the drift time is known for each hit. However no recombination correction is applied as the $\frac{dE}{dx}$ information is inaccessible at the hit level.
3. The 3D average energy direction is fitted from the 2D measurements by building a χ^2 from the differences between the observed 2D angle and

projected 3D direction in each view. Indeed, only 2 independent measurements would be necessary to reconstruct a 3D direction, and the fitting procedure allows to find the best compromise between the 3 existent plane measurements.

This whole process is illustrated in Fig. 15 where the true neutrino direction projected on the 2D planes (θ_y^{view}) as well as the reconstructed neutrino direction after the χ^2 fit projected on the 2D planes ($\hat{\alpha}^{\text{view}}$) are shown for comparison.

3.4.2 Results

All the resolutions hereafter are shown for θ_y^{true} , the zenith angle (angle of the neutrino with the upward y direction) and are calculated with the quartiles method applied on the absolute difference in the reconstructed θ_y^{true} angles. All the results discussed (and figures shown), referred for convenience as for neutrino interactions, are for particles and antiparticles of the same flavor combined, as it was checked that the performance in the two cases is comparable.

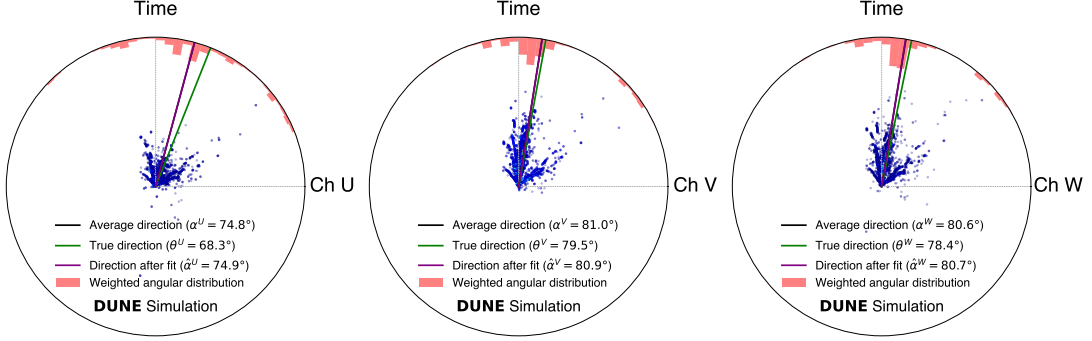


Fig. 15: Example of the calorimetric based direction reconstruction showing the direction estimation for a simulated NC interaction with 12 GeV of visible energy. This higher energy interaction was selected for illustration purpose even though it is not used in the analysis.

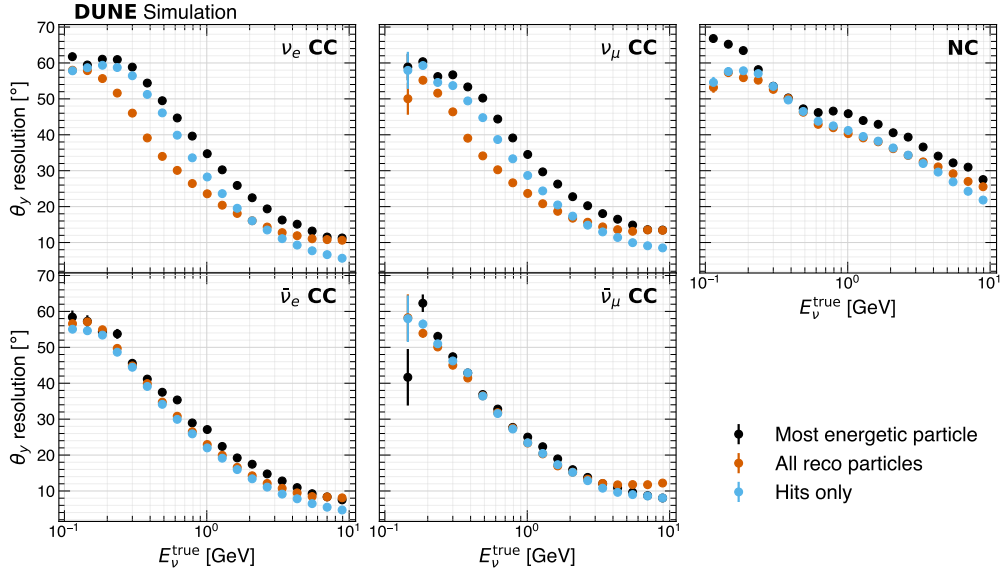


Fig. 16: Resolution (in degrees) of the reconstructed particle (Top) and antiparticle (Bottom) direction, as a function of their true energy for ν_e (Left) and ν_μ (Middle) CC interactions, and NC interactions (Right).

The obtained angular resolutions with the three methods for all the ν_e CC, ν_μ CC, $\bar{\nu}_e$ CC, $\bar{\nu}_\mu$ CC and NC interactions are presented in Fig. 16, which shows that the angular resolution improves with energy for all the methods, as expected by the relative decrease of the nucleon Fermi momentum with respect to the neutrino energy. At low energy, the momentum of the nucleon inside the argon nucleus, on which the neutrino interacts,

is relatively high with respect to the momentum of the neutrino itself. As a consequence, the momentum of the final state particles is equal to the sum of the momentum of the incoming neutrino and of the target nucleon which leads to a smearing of the initial neutrino direction. It thus becomes impossible to accurately reconstruct the neutrino direction at low enough energies. Figure 16 also shows that the method using all

the reconstructed particles systematically outperforms the method using only the most energetic particle, demonstrating the advantage of reconstructing the hadronic system that is possible in DUNE. However, these two methods converge at higher energies as the reconstruction deteriorates and tends to cluster together all the hits into a single large shower. This improvement is much stronger for neutrinos compared to anti-neutrinos given that the visible energy in the hadronic system is much lower for anti-neutrinos due to the presence of a primary neutron in the final state (*vs.* a primary proton for neutrinos) and the lower interaction inelasticity. This lower inelasticity also has the effect of improving the correlation between the lepton and neutrino direction, hence leading to very similar performance overall for the best reconstruction method for neutrinos and anti-neutrinos at a given energy. As expected, the hits-only method underperforms the all-reconstructed particles at lower < 1 GeV energies, and outperforms for higher > 2 GeV energies for neutrinos. Indeed, at lower energies the missing information about the relative masses from the particles impairs the performance of the hits-only method, while this effect is reduced at higher energies where it is compensated by the easier handling of complex topologies by removing the need for a performant high-level reconstruction of tracks and showers. The performance for NC interactions are worse than for CC interactions, as expected given that the neutrino only transfers part of its momentum in the interaction. For these interactions, the hits-only methods is the one that performs in average the best as expected by the fact that there is no primary lepton to reconstruct and several small energy deposits not forming tracks or showers.

The same resolutions are shown as a function of the (anti-)neutrino direction with respect to the zenith direction ($\cos \theta_y$) in Fig. 17. All the methods display the same behavior as a function of the neutrino direction: the best resolutions are obtained for the neutrinos orthogonal to the zenith direction while the most degraded resolutions are obtained for up-going and down-going neutrinos. This can be once again explained by the alignment of the vertical direction with the collection plane wires, inducing a loss of resolution for particles traveling in that direction.

A study was carried out on the direction resolution as a function of the calorimetric reconstructed neutrino energy for events with a single and more than one reconstructed particle. The results were used to build a hybrid direction reconstruction procedure, that applies one of the three mentioned methods depending on the number of reconstructed particles and the reconstructed neutrino energy. The hits-only method was found to be the best in almost all cases where a single particle is reconstructed, therefore chosen to be used in the hybrid model for these cases. For CC events in which multiple particles are reconstructed, an applicability threshold of 1.3 GeV in reconstructed calorimetric energy is decided: below it, the method based on reconstructed particles is applied, and the hit-based method above it. Similar events tagged as NC will always use the hit-based method. The results obtained with this hybrid method are shown in Fig. 18. It can be seen that the performance is rather independent of the full containment of the interaction, except for NC interactions for which the containment and transferred energy are very intertwined. Additionally the obtained performance is very similar between neutrinos and anti-neutrinos. For CC interactions, the obtained performance is a resolution around 25° at 1 GeV that goes down to 7° for ν_e and 9° for ν_μ at 10 GeV. The counterintuitive slightly better performance obtained for PC events across part of the energy range can be understood by the interplay between the lepton containment and the inelasticity of the interaction which impacts the direction reconstruction. The NC interactions feature a degraded resolution as expected, but this should still be sufficient to help in an oscillation analysis, by setting total flux constraints.

3.5 Neutrino flavor determination

A convolutional visual network (CVN) has been deployed to perform image recognition with the goal of providing neutrino interaction classification in DUNE's FD modules. This kind of network is particularly suited for DUNE given the nature of the detector output that can be represented as a set of three 2D images of the neutrino interaction (one for each of the u, v, w planes). This CVN proved [45] to be highly efficient and shows high purity in the selections of electron and muon neutrino interactions on samples of beam neutrino

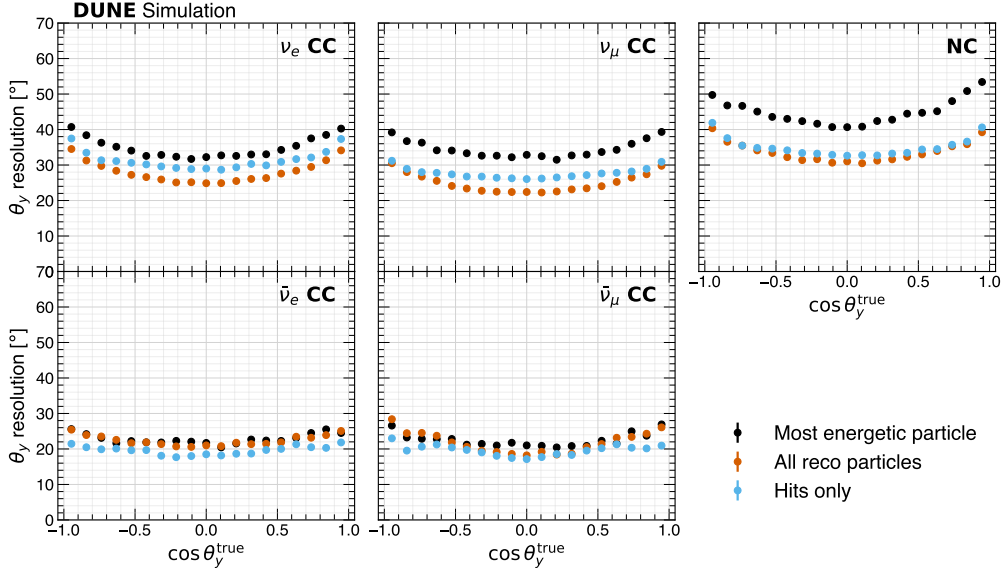


Fig. 17: Resolution of the reconstructed particle (Top) and antiparticle (Bottom) direction, as a function of the true neutrino direction with respect to the zenith for ν_e (Left) and ν_μ (Middle) CC interactions, and NC interactions (Right).

events. After it was retrained on a sample of atmospheric neutrinos, the same CVN was deployed to assess its performance on atmospheric neutrino events.

The CVN model uses as input three 300x300 pixel images/maps (one for each plane of the LArTPC), which are generated from the reconstructed 2D hits on the readout wires. A pre-selection criterion is applied to each neutrino event used for training: it must contain at least 100 hits, the neutrino energy must be less than 20 GeV, and the true neutrino interaction vertex has to be within the detector's FV (as defined in Sec. 2). This pre-selection focuses the analysis on ν_e CC, ν_μ CC, and NCs interactions, while excluding ν_τ for which a few interactions only are expected per module every year. After pre-selection, a total of 1.84 M pixel maps were used for training, 80 k for validation and 80 k for testing.

The performance is assessed on the full selected dataset according to the selections described in Sec. 2.2. For every event, the reconstructed flavor is selected as the flavor with the highest output score from the CVN. The obtained

results are shown as stacked histograms, split by true labels in Fig. 19, and split by reconstructed labels in Fig. 20. The selection efficiency for ν_μ and ν_e CC (NC) interactions is above 90 % (60 %) across the energy range, as can be seen in Fig. 19. The efficiency in selecting the CC interactions is relatively flat with the energy while there is a continuous decrease of the selection efficiency as a function of the energy for NC interactions. This can be understood by the fact that high-energy NC interactions might have similar features as CC interactions with many particles in the final state. This very same effect leads to a drop of the selection purity with the energy, as shown in Fig. 20. The lower witnessed purities and efficiencies for ν_μ CC interactions below 200 MeV can be explained by the low number of ν_μ able to undergo CC interactions due to phase space suppression, as well as by the low energy of the produced muon. The interaction containment was tested to have a minimal impact on the performance, once disentangled from the amount of transferred momentum.

Figure 21 demonstrates that the performance from the CVN is rather independent from the direction of the neutrino. The overall obtained

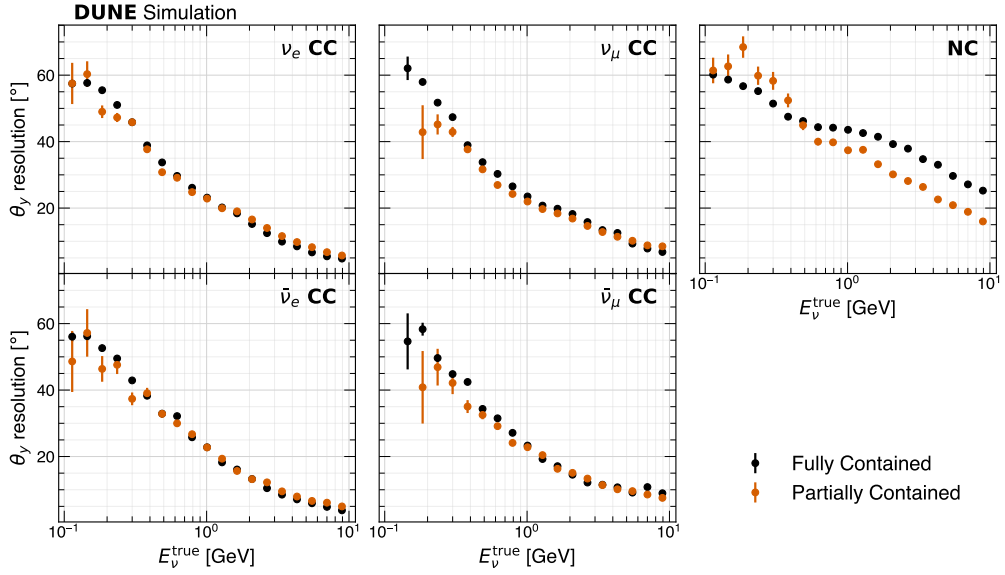


Fig. 18: Resolution (in degrees) of the reconstructed particle (Top) and antiparticle (Bottom) direction as a function of the true neutrino energy for ν_e (Left) and ν_μ (Middle) CC interactions, and NC interactions (Right), using the hybrid reconstruction method.

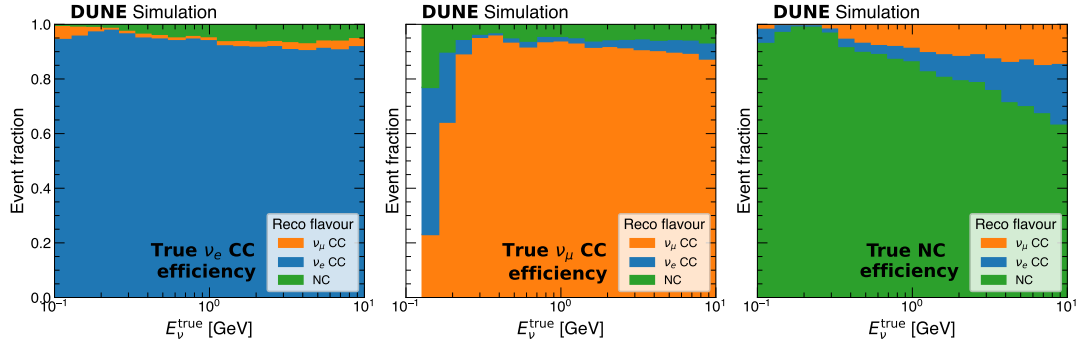


Fig. 19: Decomposition of true neutrino interaction types as reconstructed CVN types, for ν_e CC (Left), ν_μ CC (Middle), and NC (Right), as a function of the true neutrino energy.

performance is comparable to what was previously described for beam events [45], with some slight loss in performance as the pattern recognition becomes intrinsically more difficult when neutrinos can arrive from any direction, with a difficult generalization to the multiple incoming directions, and with a wider energy flux.

4 Summary and discussions

4.1 Vertex

The current DUNE vertex reconstruction algorithm for atmospheric neutrino events:

- provides a sub-cm level position resolution over a wide energy range;

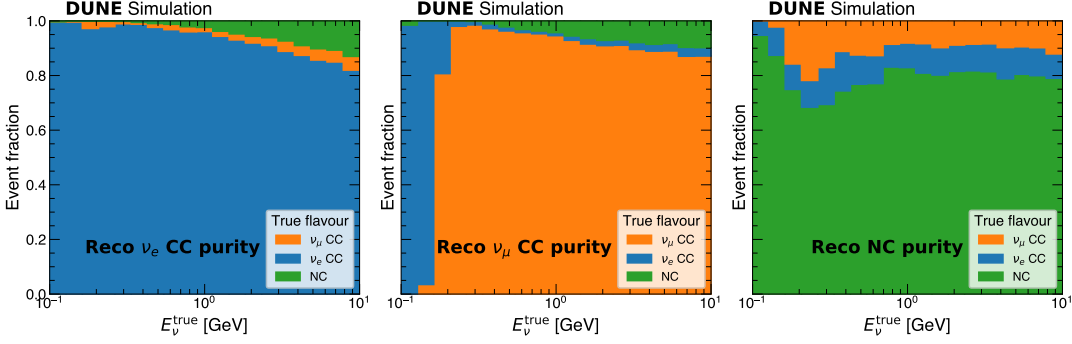


Fig. 20: Decomposition of reconstructed CVN types as true neutrino interaction types, for ν_e CC (Left), ν_μ CC (Middle), and NC (Right), as a function of the true neutrino energy.

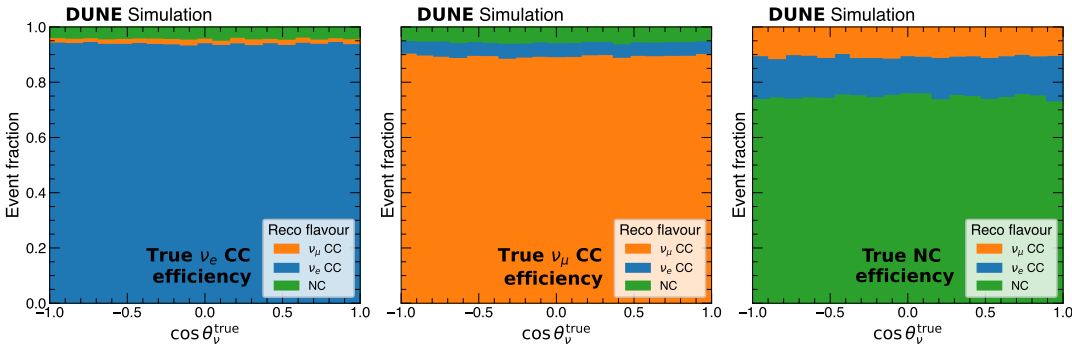


Fig. 21: Decomposition of reconstructed CVN types as true neutrino interaction types, for ν_e CC (Left), ν_μ CC (Middle), and NC (Right), as a function of the true neutrino angle with the zenith direction ($\cos(\theta_y^{\text{true}})$).

- has an efficiency (*i.e.*, the fraction of events with sub-cm resolution) depending on the neutrino energy, between 75 % to 90 % for CC fully contained events;
- has a strong energy and neutrino direction dependence of the efficiency on the y axis, understood to be caused by the FD design (*i.e.*, wires pitch and orientation in the planes of the APAs).

The performance (resolutions and efficiency of reconstructing a vertex within 1 cm of the true vertex) is similar to that obtained for the beam sample [33]. The efficiencies are higher than 80% across all energies and zenith angles in x and z directions. The lowest efficiency is found for the y direction (the direction along which the collection plane's wires are oriented along, therefore

providing less spatial resolution), where the efficiency drops to $\sim 76\%$ at low-E (<1 GeV) and all zenith angles. To improve even further these efficiencies, a possible approach is to modify in some way the current network: either modify its architecture/settings or change the type of the network itself (*e.g.*, use a graph neural network instead or in combination with the present U-ResNet).

4.2 Particle reconstruction

The *particle reconstruction efficiency* depends on both the energy and the type of the particle:

- for muons and electrons, the reconstruction efficiency is above 90% and rather flat from ~ 0.6 GeV up to 10 GeV momentum range;
- protons (pions) start with an efficiency around 90% (80%) between ~ 0.6 GeV and ~ 1 GeV,

which decreases steadily up to 60% at ~ 10 GeV after;

- for photons, the efficiency as a function of momentum is between 65% and 85% from 0.2 GeV to ~ 1 GeV, increasing after to approach $\sim 100\%$ at ~ 10 GeV.

While the best resolution for the *particle direction reconstruction* is obtained for muons, which have a resolution below 5° at a kinetic energy ($E_{\text{kin}}^{\text{true}}$) of 1 GeV, similar trends can be observed for all particle types:

- the resolution is relatively poor at low- $E_{\text{kin}}^{\text{true}}$ (below 100 MeV), in particular for proton tracks, which span $\mathcal{O}(\text{cm})$ at these energies;
- the best resolution for shower-like particles is obtained for $E_{\text{kin}}^{\text{true}}$ between 100 MeV and 1 GeV;
- at higher $E_{\text{kin}}^{\text{true}}$ the resolution degrades for shower-like particles, as events become more crowded, and the accuracy in the reconstruction of the individual particles decreases.

The *particle energy resolution* depends on the particle-type:

- Muons: DUNE can measure the contained-muons' energy with $\sim 2\%$ resolution with the CSDA method. For uncontained muons, the energy can be estimated through a MCS measurement, with the obtained resolutions highly dependent on the contained track-length and slightly on the track direction;
- Charged pions: out of the two methods studied, the CSDA performs better (but can fail catastrophically in the case of bad PID). The obtained $>\sim 30\%$ resolution is limited by inelastic hadronic interactions.
- Protons, compared to pions, exhibit a few differences: the hadronic interactions manifest at higher $E_{\text{kin}}^{\text{true}}$ values (> 1 GeV); there are more significant gains with the CSDA method. There is good resolution at low- $E_{\text{kin}}^{\text{true}}$: $< 15\%$ below 400 MeV;
- Electrons: at low- $E_{\text{kin}}^{\text{true}}$ (< 400 MeV), the resolution is limited by shower particles detection thresholds (soft electrons); at mid- $E_{\text{kin}}^{\text{true}}$ (0.4 – 1.2 GeV), the resolution is better than 10%; at high- $E_{\text{kin}}^{\text{true}}$ (> 2 GeV), the resolution degrades because of over-clustering of hits.

Particle identification in DUNE reaches a good separation between track-like and shower-like particles by selecting track-like particles with an efficiency of 89% while rejecting 91% of the showers. A particle identification is also performed over the tracks, allowing to tag protons by using a simple PIDA technique ($\frac{dE}{dx}$ profile): they can be selected with an efficiency (purity) of $\sim 87\%$ (91%). An accurate discrimination between charged pions and leptons can be achieved only when/if additional criteria (*e.g.*, the track scattering to the track length) are considered.

4.3 Neutrino energy reconstruction

The reconstructed neutrino energy

- has a resolution that varies between 10% and 20% depending on the event flavor, energy, and containment;
- depends on the true energy due to containment and interaction topologies;
- depends loosely (sub-leading order) on the neutrino direction.

The current energy reconstruction is relatively simple and relies heavily on the estimation of the hadronic energy through the measurement of the total deposited charge. Using PID information for the energy reconstruction should allow to improve these resolutions as demonstrated in [43] by using more precise energy reconstruction methods such as CSDA. Additionally, using the 3D reconstruction of the track-like particles, instead of the 2D hits calorimetry, would allow to apply recombination corrections matching the measured $\frac{dE}{dx}$ profile of each particle instead of an average recombination factor. However, despite the imperfections of the determination of the hadronic energy in the current reconstruction, the information it brings is already enough to considerably improve the energy resolution with respect to only using the primary lepton information. This is clearly demonstrated in Fig. 22, that shows a direct comparison of the energy resolution performance in two cases:

- The true lepton energy is used and rescaled at best to be unfolded into a neutrino energy by minimizing the bias, thus representing the resolution obtained with an idealized detector only accessing the lepton information;

- The reconstructed neutrino energy from the reconstructed hadronic and leptonic quantities as presented in Sec. 3.3.

At lower energies (100 MeV to 400 MeV), there is no improvement on the energy resolution brought by the detection of the hadronic system for anti-neutrinos as expected by the fact that it mainly consists of a primary neutron which is undetected. For ν_e there is however some gain from 5 % to 10 % on the absolute resolution with the detection of the hadronic system, mainly through the detection of the primary proton. A similar effect can be witnessed for ν_μ with an additional small decrease in performance at very low energies (<200 MeV), possibly due to the complexities introduced by very low-energy muons. At higher energies, the gains in resolution become more obvious. The absolute neutrino energy resolution is for example halved going down from $\sim 40\%$ to $\sim 20\%$ around 1 GeV for ν_e . A very important gain is also seen for $\bar{\nu}_e$ even though slightly less important as the share of the energy going into the hadronic system is smaller for anti-neutrinos. For ν_μ and $\bar{\nu}_\mu$ similar conclusions can be drawn. The main difference being that at higher energies, around 10 GeV, using only the true lepton information yields similar resolutions as using the full reconstructed system for $\bar{\nu}_\mu$. This is because using the true muon energy has the same effect as measuring the hadronic system. But at those energies, the muon is uncontained, and its energy is imperfectly estimated through the MCS method.

4.4 Neutrino direction reconstruction

Three direction reconstruction methods have been developed and studied for the atmospheric analyses: using lepton-only information, using all reconstructed particle, and using just reconstructed hits.

- At low-E (<1 GeV) in CC interactions, using all reconstructing particles provides the best resolution;
- At high-E, in CC interactions, a pointing resolution $\sim 5^\circ - 10^\circ$ is obtained at 10 GeV with the hits-only method;
- For NC interactions, some pointing capabilities exist, $\sim 20^\circ$ at high-E and $\sim 40^\circ$ at 1 GeV;

- The direction resolution is dependent on the direction itself for all the methods.

The poor resolutions obtained at low energy can hardly be mitigated by any reconstruction means, because of the irreducible Fermi motion. However, the resolution limit has not been reached yet, and some newer methods relying on machine learning techniques (*e.g.*, CNNs) might prove to be more efficient at reconstructing the neutrino direction.

To visualize what are the physical boundaries for any future improvements, Fig. 23 compares the neutrino direction resolution obtained with the hybrid-method for three settings: current implementation, when the 3-momentum of every used Pandora reconstructed particle is perfectly determined, and for the case in which all true final state particles (except the neutrons) are perfectly reconstructed. First, it can be seen that improving the current PID and energy reconstruction alone, without improving the lower-level reconstruction of Pandora (*e.g.*, hits, clusters, PFP, *etc.*), would only provide a relatively small improvement in neutrino direction resolution. Second, Fig. 23 shows that an ideal particle reconstruction (estimated by using all primary Geant4 particles true momentum, except the neutrons) could only provide a sizable increase in performance below 1 GeV, being already close to the current performance at higher energies. The limit is set by the inability to detect neutrons and the irremediable presence of nuclear effects. So at best, any sophisticated machine learning method could only try to approach this limit. However, ongoing development of Pandora is looking to deliver improvements in the lower-level reconstruction.

4.5 Neutrino flavor determination

An overall good performance of the CVN was obtained, with $\sim 90\%$ selection efficiency at tagging the neutrino flavour, over the whole 0.1–10 GeV energy range studied for CC interactions, with a purity above 90 % below 1 GeV and above 80 % up to 10 GeV. No significant bias of the CVN with respect to the zenith angle was observed: the selection purities are similar for all directions. Overall, the retrained-CVN performance is similar to that obtained in DUNE on the beam samples [45].

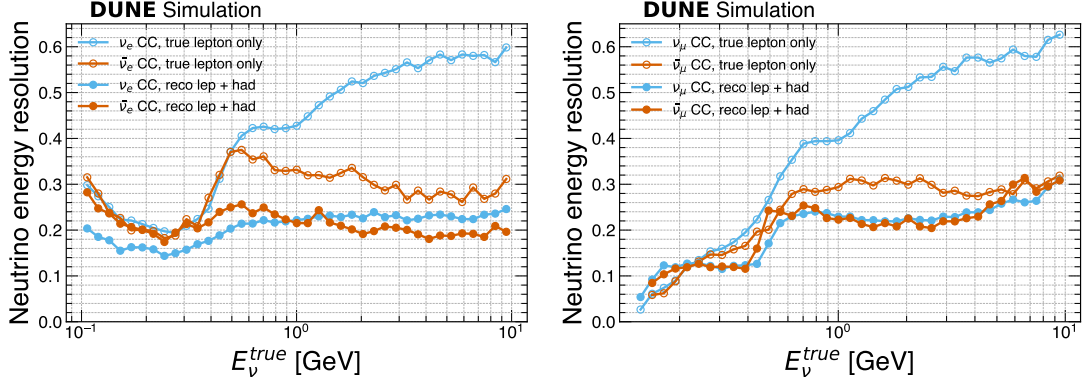


Fig. 22: Neutrino energy resolution as a function of the true neutrino energy for $\nu_e/\bar{\nu}_e$ (Left) and $\nu_\mu/\bar{\nu}_\mu$ (Right), using the true lepton energy on the one hand, and the reconstructed leptonic/hadronic energies on the other hand.

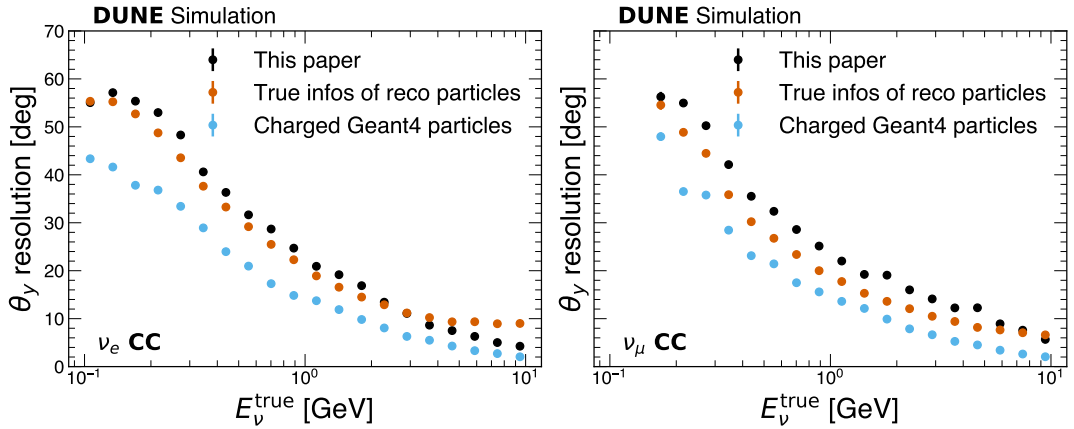


Fig. 23: Resolution in degrees on the reconstructed neutrino direction as a function of the true neutrino energy for ν_e (Left) and ν_μ (Right) CC interactions using the hybrid reconstruction method, for three cases: current implementation, when the 3-momentum of every used Pandora reconstructed particle is perfectly determined, and for the case in which all true final state particles (except the neutrons) are perfectly reconstructed.

5 Conclusions

In this paper, the reconstruction performance of atmospheric neutrinos interacting in the LArTPC horizontal drift module of the DUNE Far Detector has been presented. For the first time in DUNE, a full simulation and reconstruction chain has been deployed to study atmospheric neutrinos with energies between 0.1 GeV and 10 GeV. The Pandora pattern-recognition software package was used for vertex and particle reconstruction, with additional packages being deployed

for higher level reconstruction (*e.g.*, PID, pattern recognition, neutrino flavor identification). To optimise the reconstruction for atmospheric neutrinos, the standard accelerator reconstruction chain was modified in a number of targeted ways. First, a retraining on an atmospheric sample was done for the CNN and CVN networks used for vertexing and neutrino flavor determination algorithms, respectively. Then, improvements were brought to existing PID and energy reconstruction algorithms. Finally, specific for atmospheric event

reconstruction, was the development of additional packages to determine particle direction (including that of neutrinos).

The reconstruction efficiencies and resolutions results presented show a generally weak dependence on direction. Moreover, despite being a detector optimized for long-baseline reconstruction, it was demonstrated that the DUNE FD LArTPC technology delivers a demonstrably comparable (in overlap regions) and competitive (at lower and higher energy intervals) reconstruction performance for non-beam neutrino sources as well, and over a much wider energy range.

In addition, DUNE’s unique capabilities at reconstructing the hadronic system with much lower detection thresholds than water-Cherenkov detectors allows for improved reconstructions of both neutrino energy and direction. At the multi-GeV scale, the DUNE resolution on the zenith angle is below 10° while the energy resolution is around 15%, a significant improvement with respect to the full-KM3NeT/ORCA expected resolutions [46]. Moreover, it was shown in this paper that partially contained interactions can still be reconstructed with good performance in DUNE, meaning that DUNE’s smaller size compared to that of other neutrino experiments is not expected to significantly impair reconstruction performance at those energies. All these will allow DUNE to obtain significant sensitivity to both the mass ordering and θ_{23} with atmospheric neutrino measurements.

It was also shown in this paper that DUNE is expected to perform well at detecting and measuring the energy and direction of neutrinos below 2 GeV. At these neutrino energies, the sparser nature of the Mton scale detectors, such as KM3NeT/ORCA or IceCube, make this detection almost impossible. These interactions can be detected by kton scale detectors such as SuperKamiokande [47], but in this case, the reconstruction of the neutrino direction and energy relies almost-exclusively on the lepton measurement as most of the hadronic system is under the Cherenkov thresholds. But DUNE is able to accurately detect this hadronic system and leverage it for both energy and direction reconstruction improvements, leading to energy resolutions from 10% to 20% for CC interactions, and improved angular resolution with respect to the lepton-only

case. These characteristics makes DUNE a competitive experiment to obtain relevant sensitivities to the CP violation phase δ_{CP} . Additionally, good, consistent performance across a wide range of energies and with 4π coverage should allow DUNE to probe several beyond-PMNS effects using atmospheric neutrinos.

This work lays the foundations for physics sensitivity studies with DUNE’s atmospheric neutrinos which will follow in separate future publications. The results show that atmospheric neutrinos can be reconstructed in the DUNE FDs with similar efficiency and resolutions as beam neutrinos (ν_μ , ν_e), giving confidence that they can contribute and complement the success of the DUNE’s physics program. The confirmation of increased reconstruction performance given the possibility of performing particle identification in the LArTPC, combined with the large size of the DUNE FDs using this technology, should give confidence to the neutrino community at large of robust future contributions from DUNE to the international atmospheric physics program.

6 Acknowledgements

This document was prepared by DUNE collaboration using the resources of the Fermi National Accelerator Laboratory (Fermilab), a U.S. Department of Energy, Office of Science, Office of High Energy Physics HEP User Facility. Fermilab is managed by Fermi Forward Discovery Group, LLC, acting under Contract No. 89243024CSC000002. This work was supported by CNPq, FAPERJ, FAPEG, FAPESP and, Fundaçõ Araucária, Brazil; CFI, IPP and NSERC, Canada; CERN; ANID-FONDECYT, Chile; MŠMT, Czech Republic; ERDF, FSE+, Horizon Europe, MSCA and NextGenerationEU, European Union; CNRS/IN2P3 and CEA, France; PRISMA+, Germany; INFN, Italy; FCT, Portugal; CERN-RO/CDI, Romania; NRF, South Korea; Generalitat Valenciana, Junta de Andalucía, MICINN, and Xunta de Galicia, Spain; SERI and SNSF, Switzerland; TÜBİTAK, Turkey; The Royal Society and UKRI/STFC, United Kingdom; DOE and NSF, United States of America.

References

- [1] Abi, B., et al.: Deep Underground Neutrino Experiment (DUNE), Far Detector Technical Design Report, Volume I Introduction to DUNE. *JINST* **15**(08) (2020) <https://doi.org/10.1088/1748-0221/15/08/T08008> arXiv:2002.02967
- [2] Abi, B., et al.: Deep Underground Neutrino Experiment (DUNE), Far Detector Technical Design Report, Volume II: DUNE Physics (2020) arXiv:2002.03005. <https://arxiv.org/abs/2002.03005>
- [3] Abi, B., et al.: Long-baseline neutrino oscillation physics potential of the DUNE experiment. *Eur. Phys. J. C* **80**(10) (2020) <https://doi.org/10.1140/epjc/s10052-020-08456-z> arXiv:2006.16043
- [4] Fukugita, M., Yanagida, T.: Baryogenesis without grand unification. *Phys. Lett. B* **174**(1) (1986) [https://doi.org/10.1016/0370-2693\(86\)91126-3](https://doi.org/10.1016/0370-2693(86)91126-3)
- [5] Abi, B., et al.: Supernova neutrino burst detection with the Deep Underground Neutrino Experiment. *Eur. Phys. J. C* **81**(5) (2021) <https://doi.org/10.1140/epjc/s10052-021-09166-w> arXiv:2008.06647
- [6] Abi, B., et al.: Prospects for beyond the Standard Model physics searches at the Deep Underground Neutrino Experiment. *Eur. Phys. J. C* **81**(4) (2021) <https://doi.org/10.1140/epjc/s10052-021-09007-w> arXiv:2008.12769
- [7] Abud Abed, A., et al.: Low exposure long-baseline neutrino oscillation sensitivity of the DUNE experiment. *Phys. Rev. D* **105**(7) (2022) <https://doi.org/10.1103/PhysRevD.105.072006> arXiv:2109.01304
- [8] Abud Abed, A., et al.: The DUNE Far Detector Vertical Drift Technology Technical Design Report. *JINST* **19**(08) (2024) <https://doi.org/10.1088/1748-0221/19/08/T08004> arXiv:2312.03130
- [9] Abi, B., et al.: The DUNE far detector single-phase technology. Volume IV. *JINST* **15**(08) (2020) <https://doi.org/10.1088/1748-0221/15/08/t08010>
- [10] Ternes, C.A., et al.: Neutrino mass ordering at DUNE: an extra ν bonus. *Phys. Rev. D* **100**(9) (2019) <https://doi.org/10.1103/PhysRevD.100.093004> arXiv:1905.03589
- [11] Kelly, K.J., et al.: Sub-GeV atmospheric neutrinos and CP-violation in DUNE. *Phys. Rev. Lett.* **123**(8) (2019) <https://doi.org/10.1103/PhysRevLett.123.081801> arXiv:1904.02751
- [12] Abe, K., et al.: Test of Lorentz invariance with atmospheric neutrinos. *Phys. Rev. D* **91**(5) (2015) <https://doi.org/10.1103/PhysRevD.91.052003> arXiv:1410.4267
- [13] Aartsen, M.G., et al.: Neutrino interferometry for high-precision tests of Lorentz Symmetry with IceCube. *Nature Phys.* **14**(9) (2018) <https://doi.org/10.1038/s41567-018-0172-2> arXiv:1709.03434 [hep-ex]
- [14] Abe, K., et al.: Limits on sterile neutrino mixing using atmospheric neutrinos in Super-Kamiokande. *Phys. Rev. D* **91** (2015) <https://doi.org/10.1103/PhysRevD.91.052019> arXiv:1410.2008
- [15] Chatterjee, A., et al.: Testing nonstandard neutrino matter interactions in atmospheric neutrino propagation. *Phys. Rev. D* **93**(9) (2016) <https://doi.org/10.1103/PhysRevD.93.093017> arXiv:1409.8472 [hep-ph]
- [16] Abe, K., et al.: Search for matter-dependent atmospheric neutrino oscillations in Super-Kamiokande. *Phys. Rev. D* **77** (2008) <https://doi.org/10.1103/PhysRevD.77.052001> arXiv:0801.0776
- [17] Ahlers, M., Helbing, K., Heros, C.: Probing particle physics with IceCube. *Eur. Phys. J. C* **78**(11) (2018) <https://doi.org/10.1140/epjc/s10052-018-6369-9>
- [18] Adrián-Martínez, S., et al.: Letter of intent for KM3NeT 2.0. *J. Phys. G: Nucl. Part. Phys.* **43**(8) (2016) <https://doi.org/10.1088/0954-3899/43/8/085001>

0954-3899/43/8/084001

[19] Fukuda, S., et al.: The Super-Kamiokande detector. *Nucl. Instrum. Meth. A* **501**(2) (2003) [https://doi.org/10.1016/S0168-9002\(03\)00425-X](https://doi.org/10.1016/S0168-9002(03)00425-X)

[20] Abe, K., et al.: Hyper-Kamiokande design report (2018) [arXiv:1805.04163](https://arxiv.org/abs/1805.04163)

[21] Acciarri, R., et al.: The Pandora multi-algorithm approach to automated pattern recognition of cosmic-ray muon and neutrino events in the MicroBooNE detector. *Eur. Phys. J. C* **78**(1) (2018) <https://doi.org/10.1140/epjc/s10052-017-5481-6> [arXiv:1708.03135](https://arxiv.org/abs/1708.03135)

[22] Marshall, J.S., Thomson, M.A.: The Pandora software development kit for pattern recognition. *Eur. Phys. J. C* **75**(9) (2015) <https://doi.org/10.1140/epjc/s10052-015-3659-3>

[23] Abud Abed, A., et al.: Reconstruction of interactions in the ProtoDUNE-SP detector with Pandora. *Eur. Phys. J. C* **83**(7) (2023) <https://doi.org/10.1140/epjc/s10052-023-1733-2> [arXiv:2206.14521](https://arxiv.org/abs/2206.14521)

[24] Andreopoulos, C., et al.: The GENIE neutrino Monte Carlo generator. *Nucl. Instrum. Meth. A* **614** (2010) <https://doi.org/10.1016/j.nima.2009.12.009> [arXiv:0905.2517](https://arxiv.org/abs/0905.2517)

[25] Andreopoulos, C., et al.: The GENIE neutrino Monte Carlo generator: physics and user manual. <https://arxiv.org/abs/1510.05494> (2015)

[26] Agostinelli, S., et al.: Geant4—a simulation toolkit. *Nucl. Instrum. Meth. A* **506**(3) (2003) [https://doi.org/10.1016/s0168-9002\(03\)01368-8](https://doi.org/10.1016/s0168-9002(03)01368-8)

[27] Allison, J., et al.: Geant4 developments and applications. *IEEE Transactions on Nuclear Science* **53**(1) (2006) <https://doi.org/10.1109/tns.2006.869826>

[28] Allison, J., et al.: Recent developments in Geant4. *Nucl. Instrum. Meth. A* **835** (2016) <https://doi.org/10.1016/j.nima.2016.06.125>

[29] Church, E.D.: LArSoft: a software package for liquid Argon time projection drift chambers. <https://arxiv.org/abs/1311.6774> (2013). <https://doi.org/10.48550/ARXIV.1311.6774>

[30] Church, E.D.: Larsoft: A software package for liquid Argon time projection drift chambers. <https://larsoft.org/>

[31] Abi, B., et al.: First results on ProtoDUNE-SP liquid argon time projection chamber performance from a beam test at the CERN Neutrino Platform. *JINST* **15**(12) (2020) <https://doi.org/10.1088/1748-0221/15/12/P12004> [arXiv:2007.06722](https://arxiv.org/abs/2007.06722)

[32] Abud Abed, A., et al.: Design, construction and operation of the ProtoDUNE-SP Liquid Argon TPC. *JINST* **17**(01) (2022) <https://doi.org/10.1088/1748-0221/17/01/P01005> [arXiv:2108.01902](https://arxiv.org/abs/2108.01902)

[33] Abed Abud, A., et al.: Neutrino interaction vertex reconstruction in DUNE with Pandora deep learning. *Eur. Phys. J. C* **85**(697) (2025) <https://doi.org/10.1140/epjc/s10052-025-14313-8> [arXiv:2502.06637](https://arxiv.org/abs/2502.06637)

[34] Adams, C., et al.: Ionization electron signal processing in single phase LArTPCs. Part I. Algorithm Description and quantitative evaluation with MicroBooNE simulation. *JINST* **13**(07) (2018) <https://doi.org/10.1088/1748-0221/13/07/P07006> [arXiv:1802.08709](https://arxiv.org/abs/1802.08709)

[35] Honda, M., et al.: Atmospheric neutrino flux calculation using the NRLMSISE-00 atmospheric model. *Phys. Rev. D* **92** (2015) <https://doi.org/10.1103/PhysRevD.92.023004>

[36] Caratelli, D., et al.: Low-energy physics in neutrino LArTPCs. <https://arxiv.org/abs/2203.00740> (2022)

[37] Abratenko, P., et al.: Semantic segmentation with a sparse convolutional neural network for event reconstruction in microboone. *Phys. Rev. D* **103** (2021) <https://doi.org/10.1103/PhysRevD.103.052012>

[38] Acciarri, R., et al.: A study of electron recombination using highly ionizing particles in the ArgoNeuT Liquid Argon TPC. *JINST* **8**(08) (2013) <https://doi.org/10.1088/1748-0221/8/08/P08005>

[39] Groom, D.E., Mokhov, N.V., Striganov, S.I.: Muon stopping power and range tables 10 MeV–100 TeV. *Atomic Data and Nuclear Data Tables* **78**(2) (2001) <https://doi.org/10.1006/adnd.2001.0861>

[40] Agafonova, N., et al.: Momentum measurement by the multiple Coulomb scattering method in the OPERA lead-emulsion target. *New J. of Phys.* **14**(1) (2012) <https://doi.org/10.1088/1367-2630/14/1/013026>

[41] Antonello, M., et al.: Muon momentum measurement in ICARUS-T600 LAr-TPC via multiple scattering in few-GeV range. *JINST* **12**(04) (2017) <https://doi.org/10.1088/1748-0221/12/04/P04010>

[42] Abratenko, P., et al.: Determination of muon momentum in the MicroBooNE LArTPC using an improved model of multiple Coulomb scattering. *JINST* **12**(10) (2017) <https://doi.org/10.1088/1748-0221/12/10/P10010>

[43] Friedland, A., Li, S.W.: Understanding the energy resolution of liquid Argon neutrino detectors. *Phys. Rev. D* **99** (2019) <https://doi.org/10.1103/PhysRevD.99.036009>

[44] Abed Abud, A., et al.: The track-length extension fitting algorithm for energy measurement of interacting particles in liquid argon TPCs and its performance with ProtoDUNE-SP data. <https://arxiv.org/abs/2409.18288> (2024)

[45] Abi, B., et al.: Neutrino interaction classification with a convolutional neural network in the DUNE far detector. *Phys. Rev. D* **102** (2020) <https://doi.org/10.1103/PhysRevD.102.092003>

[46] Adrián-Martínez, S., et al.: Intrinsic limits on resolutions in muon- and electron-neutrino charged-current events in the KM3NeT/ORCA detector. *JHEP* **2017** (2017) [https://doi.org/10.1007/JHEP05\(2017\)008](https://doi.org/10.1007/JHEP05(2017)008)

[47] Jiang, M.: Atmospheric neutrino oscillation analysis with improved event reconstruction in Super-Kamiokande IV. *Progress of Theoretical and Experimental Physics* **2019**(5) (2019) <https://doi.org/10.1093/ptep/ptz015> <https://academic.oup.com/ptep/article-pdf/2019/5/053F01/28638877/ptz015.pdf>